UNIVERSITY OF CALIFORNIA,
IRVINE

Confirmation of Photoacidic Quantum Dots Using Electrochemical Impedance Spectroscopy

DISSERTATION

submitted in partial satisfaction of the requirements
for the degree of

DOCTOR OF PHILOSOPHY

in Chemistry

by

Jennifer A. Glancy

Dissertation Committee:
Assistant Professor Shane Ardo, Chair
Professor Reginald Penner
Professor AJ Shaka

2019

DEDICATION

To Pajohelira

TABLE OF CONTENTS

LIST OF FIGURES

LIST OF TABLES

ACKNOWLEDGMENTS

To my Dad, you've always celebrated my accomplishments and have never taken credit, but credit is due. You always encouraged me to find a way to achieve my goal no matter the obstacle. I want to say thank you for never letting me believe that failure from lack of effort was ok and for raising me to put care into anything I aimed to do no matter how small the project. My strength, perseverance, and resiliency are largely due to you.

To my best friend, Lindsey Berkhahn, you have been there every step of the way through fourteen years of education and four degrees. Although you never stopped telling me I was crazy for my path, you have always been one of my biggest supporters. No matter how down or stressed out I became, you were always there to get my head back in the game. You never let me feel sorry for myself and always believed I could get through anything life threw at me. Perkins will forever be one of the worst jobs we've had, but to me, it was one of the best because that's where I met you. Our pie sneaking days, slip and slide floors, and couch dumpster diving will always be some of my favorite memories. You're stuck with me for life, lady.

Claudia, my grad school roomie, there were times we didn't think we'd make it out, but we did it!!! You listened to my ranting and raving on countless occasions and you were always encouraging and supportive no matter how crazy I sounded. I'll miss our protein-shake dancing days and our whiskey and Netflix dates but we're onto bigger and better things. May we never forget, that today is for us!

Thank you to my research advisor, Dr. Shane Ardo, for taking me on as a third year. You offered constant encouragement on data no matter how daunting the results seemed and for every failed attempt, offered a dozen more ideas to accomplish what we set out to do. You bring a level of

passion and excitement to the field of solar energy that is unequaled anywhere else. I'm pretty sure if anyone called you in the middle of a night with a 'science emergency', you would either answer or call back within minutes ready to tackle the problem. I hope that excitement never wavers in your career, but I do hope you start to get more sleep!

I would like to thank Dr. Ramesh Arasasingham for the encouragement you gave, the confidence you instilled in me, and for being an example of what I aspire to be as an educator and professional. You spent time listening to my ramblings on teaching, gave me advice on how to become a more effective instructor, and gave me the assurance that I needed to believe in my own abilities. I will forever be grateful.

To Dr. Kim Edwards, thank you for the support and mentorship you provided when I needed guidance. You are a strong leader to follow and I appreciate all the work and care you put into your role as an educator. Thank you for always having my back.

To all my current and former lab mates in the Ardo group: Leanna Schulte, Eric Schwartz, Kevin Tkaczibson, Simon Luo, Joseph Cardon, Rylan Kautz, Cassidy Feltenberger, Zejie Chen, Margherita Taddei, Will White, Claudia Ramirez, Bill Gaieck, Rohit Bhide, Nazila Farhang, Dr. Sam Keene, Dr. David Fabian, Dr. Larry Renna, Prof. Jingyuan Liu, Dr. Chris Sanborn, thank you so much for being supportive, understanding, and great team players.

Additionally, I want to thank Dr. AJ Shaka and Dr. George Miller for allowing me the education and experience within the National Science and Security Consortium and for believing in me as a junior graduate student. Working with you both in the first couple of years holds some of the highlights of my graduate degree. To Alan Heyduk, thank you for giving me a place in your lab the

first summer I was here. You were an excellent mentor and supporter and I value the time you gave me immensely.

To the Chemistry department at University of West Florida and my advisor, Dr. Pamela Benz, thank you for understanding and aiding my work-education balance and for providing scholarships, research, and job opportunities which helped me to earn my degree. I wouldn't be here if not for you.

Lastly, I want to thank all the staff members in the Chemistry department, particularly Haleema Sood, Tenley Dunn, Stacie Tibbets, Jaime Albano, and Terri Short, for always being so incredibly helpful and prompt whenever I had questions or concerns. Thank you to the former director of the mass spectrometry facility, John Greaves, for the conversations on mass spectrometry and for sharing mystery novels with me my first summer of grad school. ou helped make my transition into grad school that much easier.

To Dima Fishman in the laser spectroscopy facility, you were always extremely helpful and supportive and want nothing more than to help further the science of every student you work with. Whenever our paths crossed, you consistently asked for updates on my progress and offered direct, sincere encouragement which helped me tremendously. I always went back to lab with more motivation and confidence. You are greatly appreciated.

I would also like to thank sources of funding that have helped support me and my research throughout my graduate school tenure: The National Science Foundation Graduate Research Fellowship under Grant number DGE-1321846 and the School of Physical Sciences at the University of California, Irvine.

CURRICULUM VITAE

Jennifer A. Glancy

EDUCATION

Ph.D., *Analytical Chemistry* — *2019*
University of California, Irvine — Irvine, CA
GPA: 3.91/4.00

M.S., *Analytical Chemistry* — *2014*
University of California, Irvine — Irvine, CA
GPA: 3.64/4.00

B.S., *Chemistry* — *2010*
University of West Florida — Pensacola, Fl
GPA: 3.70/4.00

A.A., *Biology* — *2008*
Santa Fe College — Gainesville, Fl
GPA: 3.85/4.00

FELLOWSHIPS AND AWARDS

Senior Lead TA — *2017 - 2018*
General Chemistry Lecture Series
University of California Irvine

Michael E Gebel Award — *2016*
University of California Irvine

Travel award to attend NSF-sponsored workshop in Santiago, Chile: — *2016*
"Photocatalysis, Photoconversion, and Photoelectrochemistry:
Fundamentals, Techniques, and Applications for the 21st Century"

National Science Foundation — *2014 - 2017*
Graduate Research Fellowship Program

Teaching assistant award — *2013*
'Contributions to the Chemistry Department Teaching Program"
University of California Irvine

Competitive Edge Fellowship — *2012 - 2013*
University of California Irvine

FELLOWSHIPS AND AWARDS *(continued)*

American Institute of Chemists Foundation Award *2011*
University of West Florida

Ralph K. Birdwhistell Scholarship *2009 - 2010*
University of West Florida

Grace Chiu Analytical Award *2009*
University of West Florida

ACS Undergraduate Award in Analytical Chemistry *2009*
University of West Florida

RESEARCH EXPERIENCE

Ph.D. Student Researcher, Department of Chemistry *2014 - Present*
University of California, Irvine Ardo Group

Projects:

1) Synthesis and characterization of cadmium selenide quantum dots towards the development of a new visible-light-absorbing photoacid. Ligand exchange of quantum dots with protonable capping ligands. Use of successive ionic layer adsorption and reaction (SILAR) on metal-oxide thin films. Material characterization by ultraviolet-visible absorption spectroscopy and acid-base titrations to quantify pK_a values. Photoacid qualification using impedance spectroscopy by measurement of proton diffusion by monitoring change in solution resistance.

2) Self-Exchange Charge Transfer between Metal-Polypyridyl Coordination Compounds Anchored to Mesoporous Metal Oxide Thin Films. Quantification and characterization of multiple-electron-transfer reactions of dyes on surface of thin film using spectroelectrochemistry.

Ph.D. Student Researcher *Summer 2014*
Lawrence Livermore National Lab Shaka Group

Project:

Develop robust characterization method for the adsorption of Fe(III) to quartz using ICP-MS and SEM to study the redox behavior of plutonium in the presence of trace iron oxide coatings on mineral surfaces.

RESEARCH EXPERIENCE *(continued)*

Ph.D. Student Researcher, Department of Chemistry *Summer 2012*
University of California, Irvine Heyduk Group

Project:
Reactivity studies of iron complexes containing the redox-active [ONO] ligand used for multi-electron small-molecule activation reactions. Particularly responsible for quantifying the organic by-products formed during these reactions through development of an analytical method using GC/MS.

Undergraduate Student Researcher, Department of Chemistry *2009 - 2010*
University of West Florida Benz Group

Project:
Study of the seasonal patterns of ultraviolet photo-protective pigments in phytoplankton in the Gulf of Mexico. Focus on the seasonal and spatial variations in the UV absorbing capacity of natural phytoplankton communities. Developed method for sample analysis of water using HPLC.

TEACHING EXPERIENCE

Head Teaching Assistant, CHEM 1C: General Chemistry Lecture *Winter 2018*
Department of Chemistry, University of California, Irvine

Head Teaching Assistant, CHEM 1B: General Chemistry Lecture *Spring 2018*
Department of Chemistry, University of California, Irvine

Head Teaching Assistant, CHEM 1A: General Chemistry Lecture *Fall 2017*
Department of Chemistry, University of California, Irvine

Teaching Assistant, CHEM 1B: General Chemistry Lecture *Summer 2017*
Department of Chemistry, University of California, Irvine

Teaching Assistant, CHEM H2A: Honors General Chemistry *Fall 2013*
Department of Chemistry, University of California, Irvine

Teaching Assistant, CHEM 1C: General Chemistry Lecture *Spring 2013*
Department of Chemistry, University of California, Irvine

Teaching Assistant, CHEM 1LE: Accelerated General Chemistry Lab *Winter 2013*
Department of Chemistry, University of California, Irvine

Teaching Assistant, CHEM 1LD: General Chemistry Lab *Fall 2012*
Department of Chemistry, University of California, Irvine

TEACHING EXPERIENCE *(continued)*

Teaching Assistant, CHM 4130L: Instrumental Analysis Lab *Fall 2010*
Department of Chemistry, University of West Florida

Teaching Assistant, CHM 3120L: Analytical Chemistry Lab *Spring 2010*
Department of Chemistry, University of West Florida

TRAINING

Public Speaking Certificate Program *May 2016*
University of California, Irvine

Course Design Certificate Program *April 2016*
University of California, Irvine

Workshop on the Application of Open Source Tools *January 2015*
for Nuclear Nonproliferation Research
University of California, Davis

Summer School on Nuclear Safeguards *August 2014*
Nuclear Science and Security Consortium
Los Alamos National Lab

Summer School in Nuclear Analytical Techniques *August 2014*
Nuclear Science and Security Consortium
University of California Davis

Summer School in Nuclear Science and Policy *August 2013*
Nuclear Science and Security Consortium
University of California-Berkeley

TAPDP- Teaching Assistant Professional Development Program *September 2012*
University of California, Irvine

PUBLICATIONS AND PRESENTATIONS

Articles

1. **Jennifer A. Glancy,** Shane Ardo. "Identification of Photoacidic Behavior Using Coupled AC and DC Electrochemical Techniques." *In preparation*.
2. **Jennifer A. Glancy**, Shane Ardo. "Demonstration of a Quantum Dot Photoacid." *In preparation.*

PUBLICATIONS AND PRESENTATIONS *(continued)*

3. Wong, Janice, Raúl Hernández Sánchez, **Jennifer Glancy**, Ryan A. Zarkesh, Joseph W. Ziller, and Alan F. Heyduk. "Disulfide reductive elimination from an iron(III) complex." *Chemical Science*. 4 (2013): 1906-1910.

Oral Presentations

1. **Jennifer A. Glancy.** "Heterogeneous Photocatalytic Systems: The Interface." 25th I-APS Meeting, Santiago, Chile. May 2016.
2. **Jennifer A. Glancy**, Hsiang-Yun Chen, Joseph M. Cardon, Jacqueline Angsono, and Shane Ardo. Studies of self-exchange electron transfer and charge accumulation at sensitized TiO_2 for multiple-electron-transfer chemistry using a series of amine-functionalized porphyrins." 251st ACS National Meeting, San Diego, CA. March 2016
3. **Jennifer A. Glancy,** Sharon Blackwell. "Seasonal Patterns of Ultraviolet Photo-Protective Pigments in Phytoplankton**."** 30th Annual Undergraduate Research Conference. University of Memphis, Memphis, TN, February 2010.

ABSTRACT OF THE THESIS

Confirmation of Photoacidic Quantum Dots
Using Impedance Spectroscopy

By

Jennifer A. Glancy

Doctor of Philosophy in Chemistry

University of California, Irvine, 2019

Assistant Professor Shane Ardo

This thesis describes the first demonstration of a quantum dot photoacid. Photoacids are a class of molecules with a protic bond that is weakened upon photo-excitation. CdSe quantum dots were synthesized and were made to have mixed-ligand surfaces with a majority of water-solubilizing sulfonate functional groups and fewer acidic electron-donor functional groups, notably 4-mercaptophenol (MPh). Sulfonate groups are very acidic and therefore remain charged over a wide range of pH values. Through judicious choice of synthesis and ligand-exchange conditions, water-solubilizing 2-mercaptoethanesulfonate (MES) was introduced in addition to an equal concentration of protic and dipolar MPh groups. The electronic states of surface-bound MPh groups are such that they can serve as electron-transfer donors to excited-state CdSe quantum dots. The challenge to characterize the photoacidity of this class of chromophores is that the charge-separated $CdSe^{-}$ and MPh^{+} state does not efficiently emit photons. Therefore, a recently developed electrochemical impedance spectroscopy technique was studied in great

detail to understand the cause of observed changes in impedance and then utilized to definitively demonstrate that this new class of quantum dot dyes were photoacidic. This light-driven energy conversion process is uniquely suited to convert light into ionic power, which can be used for direct desalination of saltwater.

DISSERTATION AT A GLANCE

Chapter 1 provides a brief introduction to the motivation of this thesis along with a brief background on solar energy, photovoltaic technologies, and photoacids.

Chapter 2 presents background on electrochemical impedance spectroscopy (EIS) and my advances to mechanistically understand the cause of observed behavior of impedance in a recently developed technique to measure photoacidity using a well-known model photoacid, 8-hydroxypyrene-1,3,6-trisulfonic acid trisodium salt (HPTS; pyranine). Notably, a large series of measurements were performed and data was critically analyzed under a simplified diffusion model to identify mechanistic causes of light-driven changes in impedance, including photo-EIS on the fully protonated and deprotonated forms of HPTS, buffer systems, with added salt, and for the non-photoacidic analog of HPTS, 8-methoxypyrene-1,3,6-trisulfonic acid trisodium salt (MPTS).

Chapter 3 reports on the synthesis and characterization of photoacid quantum dots using techniques from Chapter 2 and characterization using ultraviolet-visible absorption spectroscopy and Fourier-transform infrared spectroscopy techniques to confirm ligand speciation.

Chapter 1 **Motivation and Background on Photovoltaic Solar Energy Conversion Technologies and Photoacids**

1.1. Energy Background and Motivation

The 1970s energy crisis prompted the United States federal government to expand its research and development programs in renewable energy, such as solar, hydropower, wind, and geothermal.[1–3] Since that time the efficiency of laboratory-scale devices for solar energy conversion to electricity has grown from 22.0% for a single crystal, single-junction gallium arsenide solar cell (IBM, 1976) to 46.0% for a quadruple-junction concentrator cell (Fraunhofer ISE and Soitec, 2014).[4,5] The best research-cell efficiencies of photovoltaic technologies over the past four decades as reported by the National Renewable Energy Laboratory (NREL) are shown in Figure 1.1.[5]

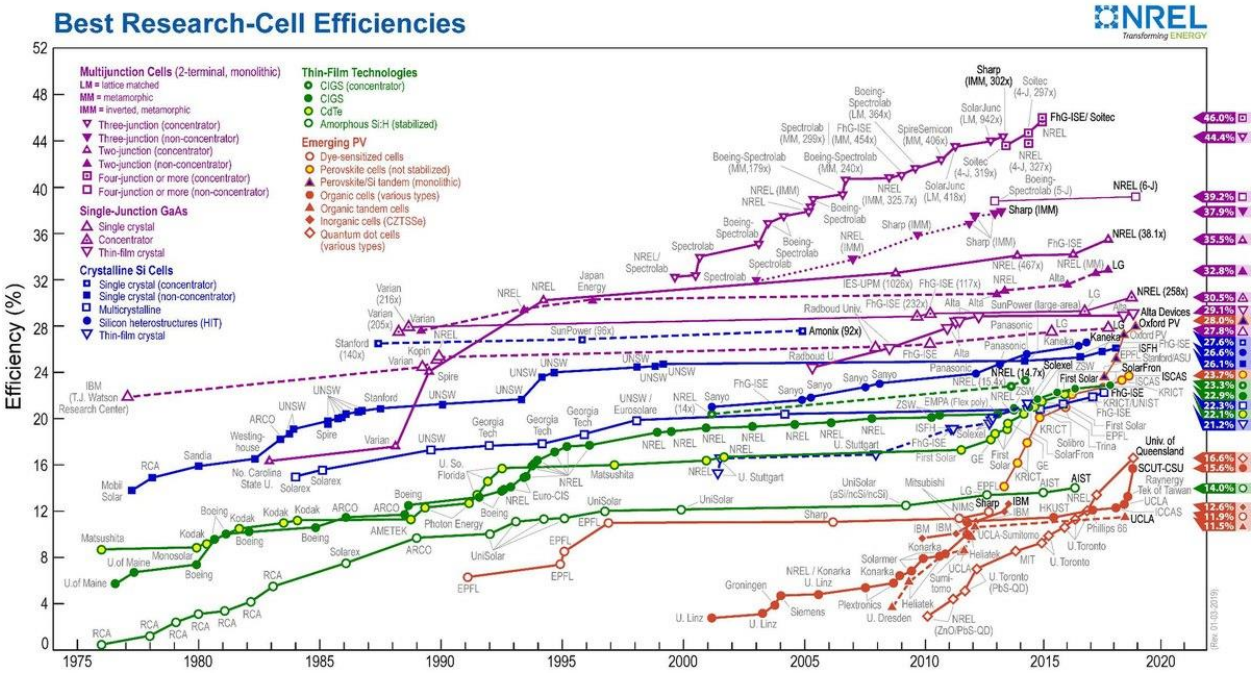

Figure 1.1 Best research-cell efficiencies of laboratory-scale photovoltaic cells.

Commercially, the majority of silicon-based solar cells exhibit efficiencies of ~17%, with the largest efficiency cells of 22% produced by SunPower.[6,7] Until recently, the cost of electricity from solar cells could not compete with the cost of electricity from fossil fuels, but in the past decade, the cost of solar photovoltaic panels has decreased by 80%, thus making solar energy a cost-effective alternative to energy from fossil fuels.[8]

Despite the fact that utilization of solar energy is increasing along with efficiency, the amount of solar energy available is going largely unused. The Sun continuously provides 1.2×10^5 terawatts of power to the Earth which is far more than that available from all renewable and nonrenewable energy sources.[4] According to the United States International Energy Agency, in 2013, humans produced and used about 5.67×10^{20} Joules of energy and in 2018, global electricity demand increased by 4% (900 terawatt hours), almost twice as fast as the overall demand for energy which includes electricity generation, preparation of fuel, and energy transport.[9,10] Although renewable energy provided 45% of this new energy, energy generation from coal-fired and gas-fired power plants also rose, increasing CO_2 emissions by 2.5%.[11]

Since the Industrial Revolution, it has been known that the supply of nonrenewable resources such as coal, natural gas, and oil were not infinite. The idea of moving toward a 100% renewable electricity supply has since been proposed and discussed; for example, in 1975 Bent Sørensen proposed such a plan for Denmark.[12] Afterward, Amory Lovins, and Bruckman, two scientific writers on energy policy, suggested a rough outline for a renewable energy future for the United States and Germany, respectively, in contrast to the expansion of nuclear energy as a replacement to fossil fuels.[13] Since then, the feasibility analyses have been much more detailed for a number of different countries on 100% renewable electricity supply options by 2050.[13–21]

For the United States, NREL has published the Renewable Electricity Futures Study where a variety of different scenarios are assessed ranging from 30% to 90% of renewable electricity.[22] The study concluded that a more flexible electric grid would be more than adequate to supply 80% of the total electricity generation in 2050 including meeting electricity demand in every region on an hourly basis.[22] These studies included the use of biomass, geothermal, hydropower, solar, and wind with nearly 50% of the total electricity generation from variable wind and solar photovoltaic generation.[23] To achieve this future, these scenarios included technology improvements for earlier stages technologies, particularly solar.[23]

1.2. Harnessing Solar Energy with Protons

Photovoltaic solar cells use sunlight to produce direct current electricity which is used as an energy source to power a load. The system relies on the photovoltaic effect, observed by Edmund Becquerel in 1839, which causes some materials to absorb photons of light and generate an electric current.[24,25] The photoelectric effect was later described in 1905 by Albert Einstein and the first photovoltaic module built by Bell Laboratories in 1954.[26] However, cost prohibited the technology from gaining widespread use until the space industry began utilizing it to power spacecrafts.[27]

Photovoltaic cells are composed of at least two layers, typically consisting of an n-type semiconductor and a p-type semiconductor. The n-type layer contains mostly (n)egatively charged electronic mobile charge carriers, which thermalize from donor dopants consisting of atoms with five valence electrons embedded within the silicon crystal lattice such as phosphorus, and the p-type layer contains mostly holes as (p)ositively charged electronic mobile charge

carriers, which are formed due to thermalization of electrons into acceptor dopants consisting of atoms with three valence electrons embedded within the silicon crystal lattice such as boron. Upon absorption of photons, electrons and holes are separated by at least one selective contact to generate a photovoltage and current flow through an external circuit as electricity.[28]

In Nature, solar energy is utilized by photosynthesis, which involves the concerted motion of electrons and protons. Protonic solar energy conversion and has been a subject of interest in solar energy research.[29–34] The idea of modeling photosynthetic solar energy conversion was first discussed over 100 years, for example, by Giacomo Ciamician in a lecture titled "The Photochemistry of the Future" where he predicted that imitating the assimilating processes of plants would artificially put solar energy to practical uses.[35,36] Modeling photosynthetic systems, this approach aims to convert the energy in solar photons into energy in chemical bonds, storing it in molecules such as hydrogen and hydrogen peroxide while also producing oxygen from water.[37–41]

Natural photosynthesis from sunlight has an upper limit efficiency of 4.5% for C3 plants or microalgae, however this is rarely observed, with the exception of sugarcane in tropical climates, and is typically found to be ~1%.[42–45] Due to the extreme complexity of natural photosynthesis, scientists aim to mimic this function via artificial photosynthesis which is less complicated and is capable of producing biofuels like methane, hydrogen gas, and alcohols, or converting carbon dioxide to carbon monoxide.[38,46,47] These studies focus on using sunlight to reduce carbon dioxide in aqueous solution to carbon monoxide, ethanol, or methane:

$$CO_2 + 2H_2O + 8h\nu \rightarrow CH_4 + 2O_2 \qquad (1)$$

or to split water, which entails two multi-electron-transfer reactions, into molecular hydrogen and molecular oxygen as follows: [48,49]

$$2H_2O + 4h\nu \rightarrow 2H_2 + O_2 \qquad (2)$$

$$2H_2O + 2e^- \rightarrow H_2 + 2OH^- \qquad (2a)$$

$$2H_2O \rightarrow O_2 + 4H^+ + 4e^- \qquad (2b)$$

Water electrolysis is not possible by simply illuminating water because water does not absorb sunlight and therefore photosensitizers capable of absorbing sunlight must be incorporated.[42,50,51] The most successful approach thus far has been photoactivation of solid-state semiconductor materials.[51]

Another natural process, light-driven proton pumps, are found in *Halobacterium halobium*. The protein used by Archaea, bacteriorhodopsin, is capable of using light energy to drive protons across the cell membrane where the electrochemical potential difference in the proton gradient is then converted into chemical energy.[52] Upon absorption of a photon, the photoactive retinal cofactor buried within the protein changes its confirmation from all-trans to 13-cis, Figure 1.2, which results in a change of the tertiary structure of the surrounding protein to drive the proton pumping mechanism.[53]

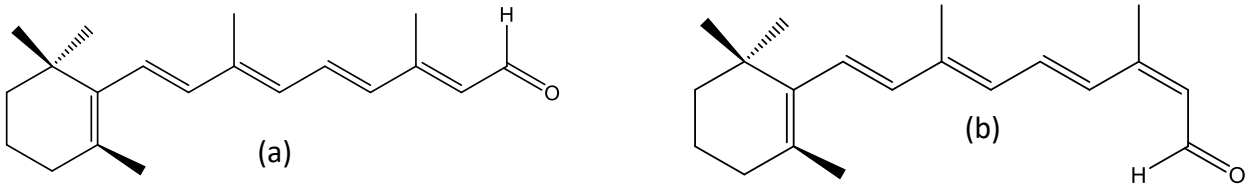

Figure 1.2 (a) all-trans-retinal and (b) 13-cis-retinal

The photocycle for bacteriorhodopsin, has been well characterized by spectroscopic and crystallographic methods.[54] Other phototrophic systems in bacteria, algae, and plants, also use proton gradients but are more indirect and involve electron transfer chains involving more proteins. Other plant systems also use additional accessory pigments to aid in capturing light which can expand the useable solar spectrum but add additional complexity. To mimic the light driven proton pump system found in bacteriorhodopsin, molecules known as photoacids can be utilized.

1.3. Photoacids

The most common photoacids are aromatic organic molecules that are weaker acids by many orders of magnitude in the ground electronic state than in their first excited electronic state.[55] The transfer of a proton to protic solvents depends on the strength of the photoacid with the weakest able to efficiently transfer a proton to water and the strongest able to transfer a proton to solvents such as dimethyl sulfoxide, ethanol, and methanol.[56–60] For weak to intermediate photoacids, the protic transfer to ethanol and methanol is found to be 3.5 orders of magnitude slower than in water. [56–58]

The light-drive proton pumping mechanism is predicated on an acid–base process that involves molecules such as a carboxylic acid R–CO_2H and its conjugate base R–CO_2^- . These species interconvert and exhibit an equilibrium constant, K_a:[61]

$$R\text{–}CO_2H \underset{}{\overset{K_a}{\rightleftharpoons}} R\text{–}CO_2^- + H^+ \qquad (3)$$

The full cycle that a photoacid undergoes following photon absorption is known as the Förster cycle and is used to determine excited-state equilibria.[62]

In the case of a photoacid, light excitation generates an excited state HA^*, that may release a proton to a greater extent than the ground state, and achieve a quasi-equilibrium defined by K_a^*:[61]

$$R(CO_2H)^* \underset{}{\overset{K_a^*}{\rightleftharpoons}} R(CO_2^-)^* + H^+ \qquad (4)$$

A common photoacid, pyranine, has a ground state pK_a of 7.7, near the pH of neutral water, and an excited-state pK_a of 1.3 making it a weak to intermediate strength photoacid. The protonated form absorbs from around 330 nm to 500 nm and has a λ_{max} at 405 nm which is only a portion of the useable solar spectrum as seen in Figure 1.3.[63] Many potential photoacid candidates absorb at even higher energies and therefore poorly absorb solar photons.

1.4. Coupling Photoacids and Quantum Dots

The goal of this thesis is to extend the region of sunlight that can be absorbed by thiol-photoacids by coupling them with cadmium selenide quantum dots. Cadmium selenide (CdSe) quantum dots absorb farther into the visible region, over 600 nm, through tuning of the synthesis procedure and reaction time.[64–66] The photo-acidic ligand used in this thesis, 4-mercaptophenol (MPh), has maximum absorbance in the high ultraviolet-visible absorption spectroscopy region at 230 nm and 270 nm. Conjugation with CdSe quantum dots extends this absorbance to ~530 nm. However, common characterization techniques for photoacids such as transient absorption spectroscopy, transient mid-infrared spectroscopy and acid–base titrations, cannot be easily utilized for characterization of thiol-coated CdSe quantum dots.[57,59,61,67–70]

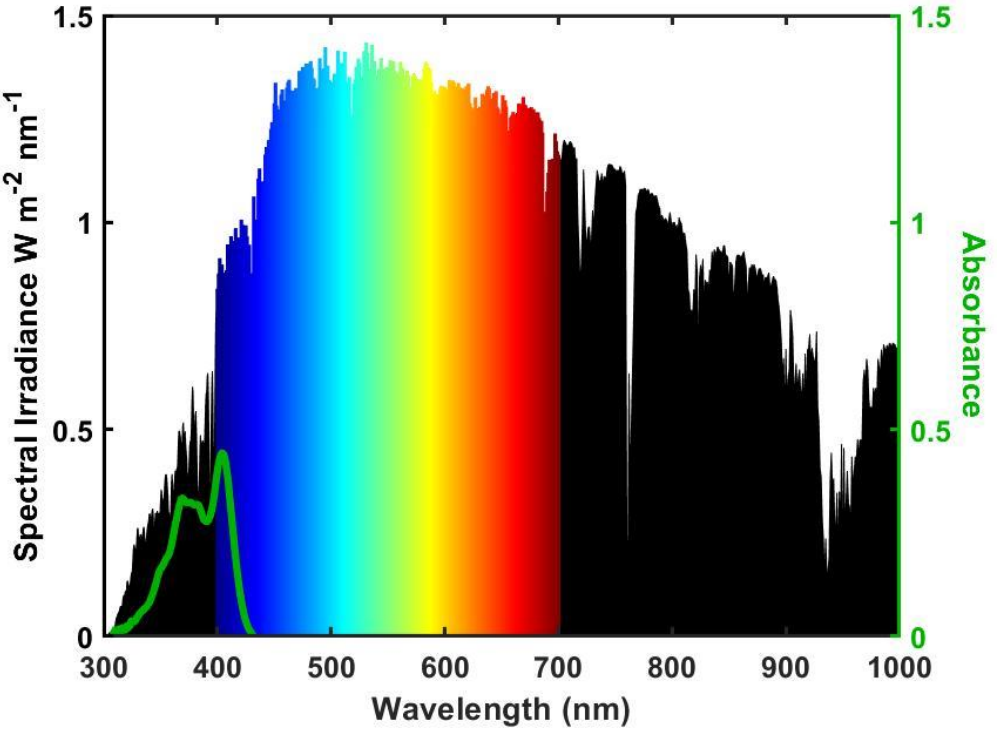

Figure 1.3 The solar spectrum at Earth's surface. The black shaded region represents the spectral irradiance in W m^{-2} nm^{-1}, the visible region is represented from 400 nm to 700 nm, and the green absorbance peak is a scaled absorbance spectrum of pyranine. Reference AM 1.5 Spectra. Data provided by the American Society for Testing Materials (ASTM) Terrestrial Reference Spectra for Photovoltaic Performance Evaluation

Thiols, particularly MPh, are known to quench the fluorescence of the CdSe, eliminating many large and easily observable transient absorption features to be used for characterization.[71–75] In addition, quantum dots are not stable at extreme pH's which eliminates acid-base titration techniques as a characterization resource.[76,77] Fortunately, it is this lack of fluorescence that will be utilized to ensure that the holes generated upon excitation in the CdSe quantum dots are transferred to the photoacidic ligand, allowing for the release of a proton. To synthesize the quantum dots, well known procedures were followed.[65,66,78–80] Characterization was done with ultraviolet-visible spectroscopy (UV-VIS), Fourier transform infrared spectroscopy (FTIR), X-Ray

diffraction (XRD), and fluorescence measurements. For the ligand exchange of oleate-capped CdSe quantum dots, literature methods were followed and in some cases were combined to yield a mixed-ligand product.[71,72,76,81,82] Fourier transform infrared spectroscopy and UV-VIS were used to confirm all ligand exchange products and will be presented.

This thesis utilizes a new method, developed by Dawlaty, et. al., to characterize the photoacidic behavior of the quantum dots using electrochemical impedance spectroscopy. The technique is sensitive to the concentration of protons upon light excitation of a photoacid, pyranine, where a significant change in impedance is observed at low frequencies between dark and light excitation. The results are supported through control measurements on water and deprotonated pyranine showing no significant change in impedance between light and dark measurements. [83]

1.5. Electrochemical Impedance Spectroscopy

Electrochemical impedance spectroscopy (EIS) is an electrochemical technique which measures the frequency dependent impedance of a system. Impedance spectroscopy can be applied to a number of applications including interfacial processes such as redox reactions, geometric effects of mass transfer or porous electrodes, battery and fuel cell analysis, biological membranes, and electrocatalytic reactions.[84–87] Analysis using impedance spectroscopy requires knowledge of complex numbers and electrical circuits, which will always contain resistance elements. Because impedance spectroscopy measures the AC and DC resistance, the opposition of electric current of a system, fundamental laws must be known: Ohm's Law and Kirchhoff's Law. Ohm's Law, representing the passage of current through a resistor:

$$V = Ri \tag{1}$$

where *i* stands for current (A), R stands for resistance (Ω), and V stands for voltage (V). This equation allows the current to be determined if the voltage is known. The first of Kirchhoff's Laws states that the sum of currents entering any point is equal to the sum of currents leaving, which equals zero:

$$\sum_k i_k = 0 \tag{2}$$

The same also applies to voltages in loops which states that the sum of voltage drops in a closed loop equals zero:

$$\sum_k V_k = 0 \tag{3}$$

Using Kirchhoff's first law, a total current, $i = i_1 + i_2$, can be used in Ohm's Law to obtain:

$$i_1 = \frac{V_a - V_b}{R} = \frac{V}{R_1} \quad and \tag{4}$$

$$i_z = \frac{V}{R_2} \tag{5}$$

In which combining them obtains:

$$i = \frac{V}{R_1} + \frac{V}{R_2} = V\left(\frac{1}{R_1} + \frac{1}{R_2}\right) = \frac{V}{R_{eq}} \tag{6}$$

Showing that an equivalent resistance can be used to represent multiple resistances giving the final equation:

$$\frac{1}{R_{eq}} = \frac{1}{R_1} + \frac{1}{R_2} \tag{7}$$

Electrical circuits often contain other elements such as capacitors and inductors. Capacitance, C, is the ability of a system to store an electric charge and is represented by a relation between the charge, Q, measured in coulombs, C, and voltage of a system where capacitance is in farads, F:

$$V = \frac{Q}{C} \quad and \tag{8}$$

$$Q(t) = \int_0^t i(t)\, dt \tag{9}$$

Inductance, L, is a property which opposes any change of magnitude and direction of electric current passing through a conductor and is used to calculate the potential difference developed by using the change of current in the system over time:

$$V(t) = L\frac{di(t)}{dt} \tag{10}$$

To find the impedance, Z, of a system, Laplace and Fourier transform are used to obtain the DC and AC impedance component for each electrical element (Table 1.1), where $s = \sigma + j\omega$, and Ohm's and Kirchhoff's Laws are used to find the total impedance.[84]

Table 1.1 Impedance equations for each element found using Laplace transform

Element	Impedance ($s = \sigma + j\omega$)	AC Impedance
R	R	R
C	$\frac{1}{sC}$	$\frac{1}{j\omega C}$
L	sL	$j\omega$L

For ideally polarized liquid electrodes, and R-C circuit is easily used to model the impedance. However, for electrodes which develop a double-layer capacitance which is not purely capacitive or represents a distribution of capacitors, another element, the constant phase element (CPE), is used to model the circuit. When the capacitance element is replaced by a CPE, it is represented as follows:

$$\hat{Z}_{CPE} = \frac{1}{T(j\omega)^{\emptyset}} \tag{11}$$

Where T is related to the electrode capacitance, in F $s^{\phi-1}cm^{-2}$ and ϕ is the constant phase element which is always between 0 and 1 which represents the deviation from a straight capacitive line from 90° by 90°(1- ϕ). The closer the value is to 1, the more purely capacitive the system.

1.5.1. Nyquist and Bode Plots

Analysis of impedance are done using Nyquist and Bode plots where the previous elements are related. A Nyquist plot, or Argand diagram, are plots of the imaginary versus real impedance. The real axis, Z_{Real} or Re(Z), corresponds to the resistance of the circuit and the imaginary, $-Z_{imag}$ or Im(Z), corresponds to the reactance of the circuit.

$$Z = \mathrm{Re}(Z) + j\,\mathrm{Im}(Z) \tag{12}$$

The plot will typically show a semicircle, representing the charge transfer resistance of the system but will often show diffusion regimes as well. The output from a parallel RC circuit is shown in Figure 1.4. The diffusion region at low frequency is typically referred to as Warburg diffusion and will be discussed shortly.

The two types of Bode plots are of the log of magnitude of impedance, log|Z| versus the log of frequency, log(*f*) and of the phase angle, ϕ, between the current and voltage versus log *f*. The magnitude of Z, |Z| is the ratio between beak current and voltage:

$$\frac{V_o}{I_o} = |Z| = \sqrt{Re(Z)^2 + Im(Z)^2} \tag{13}$$

The phase can also be found using the Im(Z) and Re(Z) components:

$$\theta = \tan^{-1}\frac{Im(Z)}{Re(Z)} \tag{14}$$

For an ideal circuit, the magnitude in the Bode plot provides two pieces of information: a constant value log|Z| = logR at high frequencies and a straight line with a slope of -1 and an inflection point giving the breakpoint frequency, ω =1/RC. The phase angle Bode plot represents the components of the circuit: a resistor will have a phase of 0° at all frequencies, a capacitor will have a phase of -90° at all frequencies, and an inductor will have a phase of +90° at all frequencies. For mixed circuits, a combination of these values are seen; for example, for a series RC circuit, the Bode plot will present a phase change from 0° to -90° as frequency is decreased, and for a parallel RC circuit, the phase changes from -90° to 0° as frequency is decreased. Non-ideal circuits will exhibit shifts from these values. The two types of Bode plots, representing phase and magnitude for a parallel RC circuit, are shown in Figure 1.4.

1.5.2. Warburg Impedance

Resistance to mass transfer, or diffusional processes, in an electrochemical cell is most often represented by Warburg impedance in equivalent circuit models. A common circuit to use, the

Randles equivalent circuit, is shown in Figure 1.5, showing R_Ω, which represents the solution resistance, C_{dl} which represents the capacitance of the diffuse–double-layer, and the substitution of the general impedance, Z_f, with Warburg impedance, Z_w, representing diffusion and the charge transfer resistance, R_{ct}. R_Ω can be thought of as the resistance to ion transport through the electrolyte, R_{ct} is related to the activation energy for charge transfer across the interface of the electrode and if species in solution do not transport fast enough to replenish at the electrode surface, Z_w describes that. Charging of the diffuse–double-layer occurs in parallel to charge transfer and is described by C_{dl}.

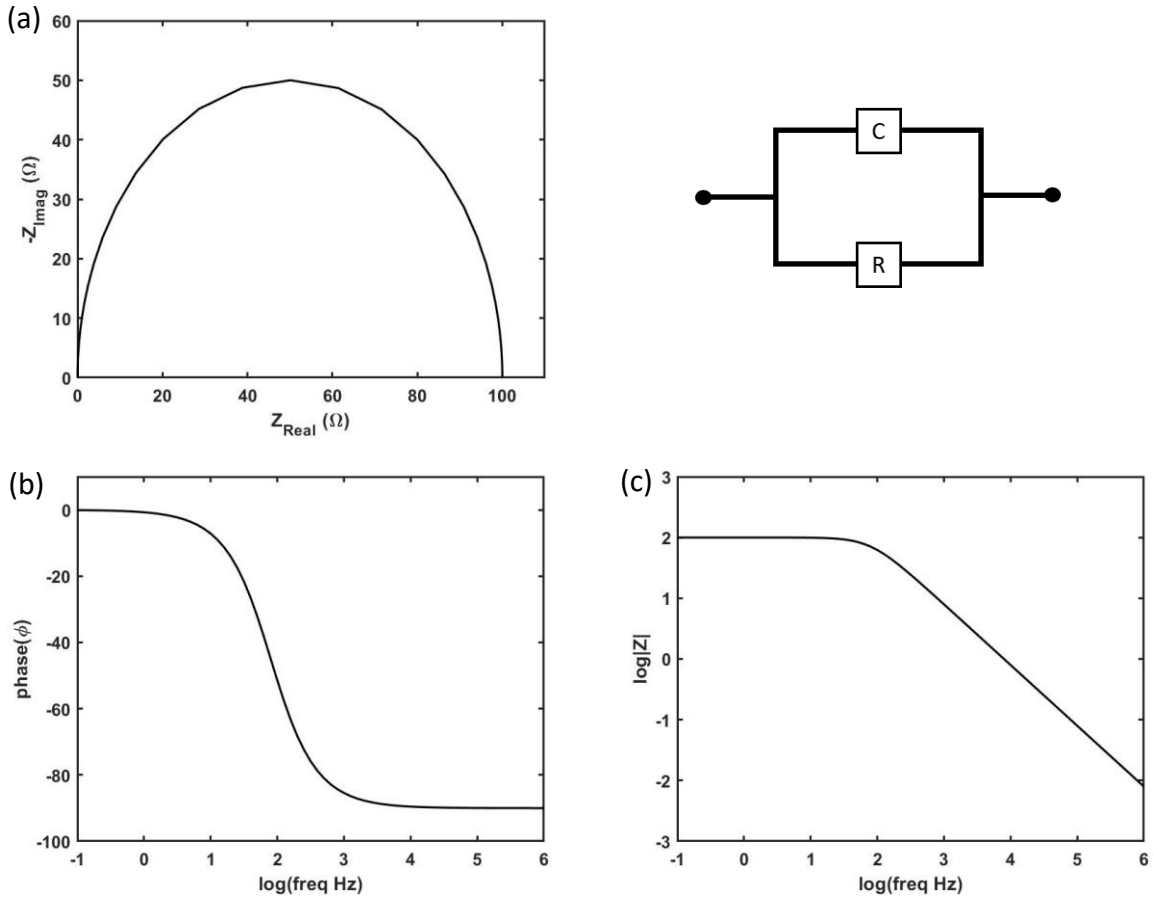

Figure 1.4 (a) Nyquist plot, (b) phase Bode plot, and (c) magnitude Bode plot for an RC circuit in parallel, R = 100 Ω and C = 20 µF, as shown.

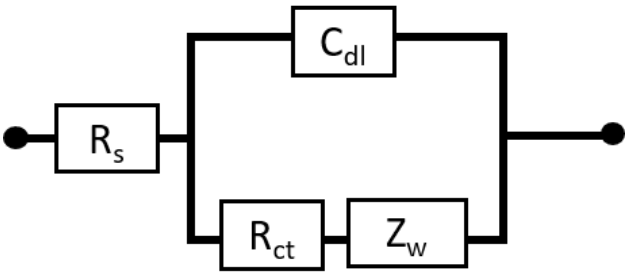

Figure 1.5 The Randles equivalent circuit representing Warburg impedance where R_s represents the solution resistance, C_{dl} represents the double layer capacitance, R_{ct} represents the charge transfer resistance, and Z_w represents the Warburg diffusive impedance.

Warburg diffusion has distinguishing characteristics in Nyquist and Bode plots as shown in Figure 1.6. In the Nyquist plot, a deviation from a full-semicircle, as seen in Figure 1.4, is shown. This deviation typically has a 45° angle to the x-axis and represents the mass-transfer regime at low-frequencies. This depth of the AC signal is shallower than the layer thickness, so at high frequencies, this is represented by the 45° angle, and at low frequencies the imaginary impedance goes to infinity because constant current cannot flow in the system.[84] Accordingly, the phase Bode plot exhibits a 45° phase shift and the magnitude Bode plot shows a slope of -1/2, similar to those shown in Figure 1.6.

However, the Warburg element assumes semi-infinite (unrestricted) linear diffusion and can deviate from ideal behavior in cases where the diffusion is restricted in finite regimes. There are two boundaries in finite-length diffusion: absorbing/transmissive and reflective. In total absorbing/transmissive boundary diffusion, the boundary affects the rate of diffusion by immediately removing/"absorbing" species whereas in reflective boundary diffusion, the boundary affects the rate of diffusion because it is impermeable to species transport and thus

"reflects" them.[88] In the case of a total absorbing/transmissive boundary, the Warburg element used is Warburg Element (short), W_s and with reflective boundary, Warburg Element (open), W_o.

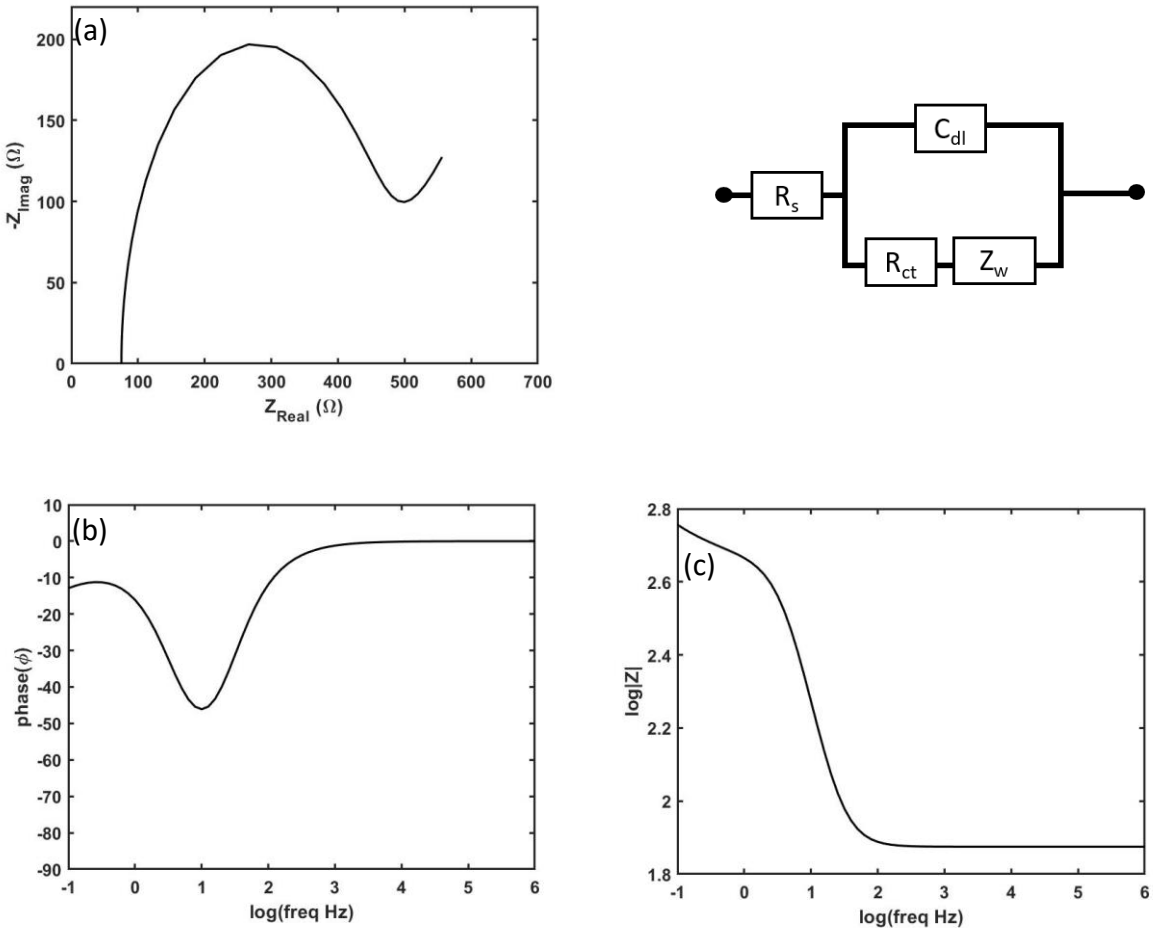

Figure 1.6 (a) Nyquist plot, (b) phase Bode plot, and (c) magnitude Bode plot representing Warburg impedance using a Randles circuit with R_s = 75 Ω, C_{ddl} = 100 µF, R_{ct} = 375, and the Warburg impedance component, Z_w = 90 $\Omega s^{-1/2}$ as shown.

For each type of finite Warburg diffusion, the expected 45° phase change shows deviation and the diffusion can be considered to be anomalous rather than ordinary linear diffusion. For anomalous diffusion, the mean squared displacement of the diffusing species do not follow the ordinary linear law[89],

$$< r2 > \propto\ t \tag{15}$$

but has a power law with dependence on time,

$$< r2 > \propto\ t^{\beta} (0 < \beta < 2) \tag{16}$$

creating a deviation from the ½ exponent law as follows:

$$Z(i\omega) \propto (i\omega)^{-1/2} \tag{17}$$

$$Z(i\omega) \propto (i\omega)^{-\beta/2}\ \ (0 < \beta < 2) \tag{18}$$

For anomalous diffusion with an absorbing/transmissive boundary, species are immediately "absorbed" at the boundary, L, meaning that the concentration at the boundary is zero and the flux across the cell is at steady-state[88–91]

$$C = 0\ (x = L) \tag{19}$$

For the impedance of a diffusive system with an absorbing boundary, the equation is as follows[88]:

$$Z(s) = R_w \left(\frac{\omega_d}{s}\right)^{\gamma/2} tanh\left[\left(\frac{s}{\omega_d}\right)^{\gamma/2}\right] \tag{20}$$

where R_w is the diffusion resistance, s is the Laplace variable related to angular frequency (iω), and D is the diffusion coefficient in $cm^2\ s^{-1}$, γ is the anomalous diffusion exponent, and ω_d is the frequency of diffusion in a finite layer which corresponds to transit time to cover the distance, L, in rad s^{-1}:

$$\omega_d = \frac{D}{L^2} \tag{21}$$

at high frequencies, for γ < 1,

$$Z(s) = R_w \left(\frac{\omega_d}{s}\right)^{\gamma/2} \tag{22}$$

and at low frequencies, a parallel combination of a resistance and a CPE where $Q = 3R_w\omega_d^{\gamma}$:

$$Z(s)^{-1} = \frac{1}{R_w} + \frac{1}{(Qs^{-\gamma})} \tag{23}$$

This arises because polarization of the working electrode in this regime is influenced by and affects the other far absorbing boundary and therefore the capacitance of the other side must be included in the model in addition to a diffusional resistance to mass transport.[87]

Using this information, the circuit model for the Warburg Element (short) can be represented as shown in Figure 1.7a where the diffusive Warburg element in the Randles circuit of Figure 5, has been replaced by a parallel RC circuit. The double layer and parallel diffusion capacitances are substituted for constant phase elements, representing the imperfect capacitance of the system as shown in Figure 1.7b. Furthermore, in two-electrode electrochemical measurements both electrodes are being polarized and influenced at all frequencies and thus at low frequencies when the diffusion layer reaches the other electrode, no additional interfacial capacitance is being introduced. Thus, the parallel diffusion constant phase elements is removed from the equivalent circuit diagram leaving two resistors in series, R_{ct} and R_{diff}, which add together to form the total charge transfer and mass transfer diffusional resistance. The final simplified circuit model is shown in Figure 1.7c.

The following chapter, Chapter 2, will present an investigation of an impedance technique to characterize photoacids using this simplified circuit model. The technique is then used to characterize newly synthesized photoacidic quantum dots in Chapter 3.

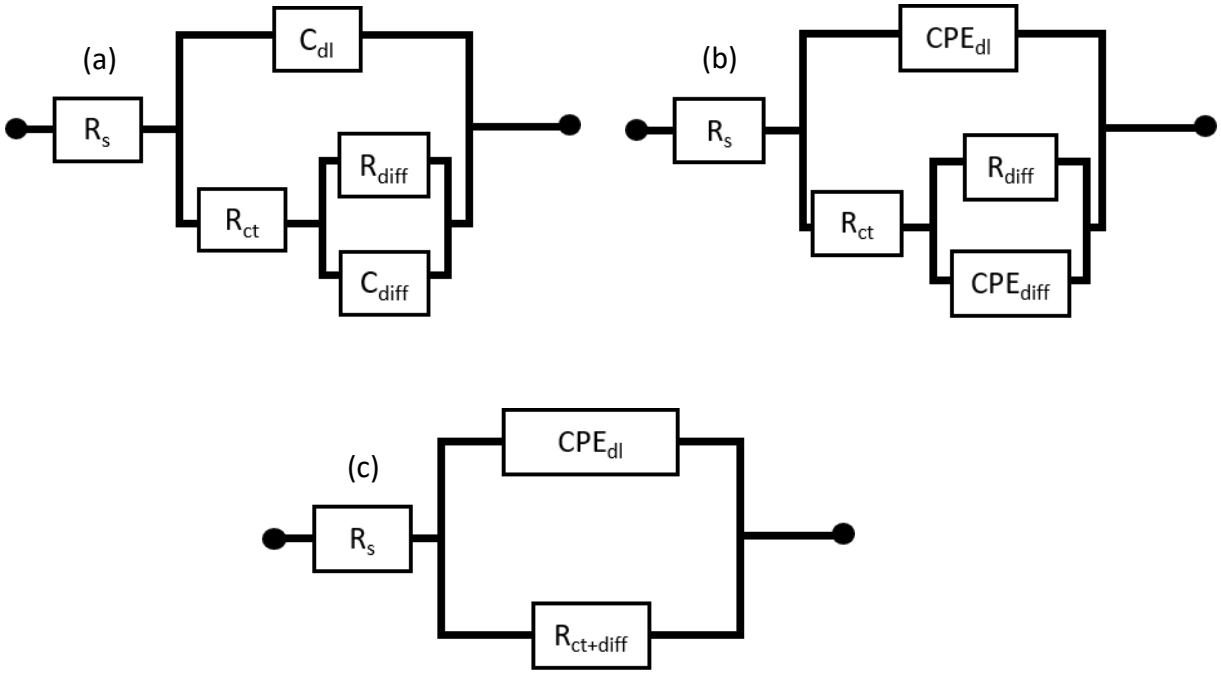

Figure 1.7 (a) Randles circuit for one electrode with the Warburg element substituted for a resistor, R_{diff}, and capacitor, C_{diff}, in parallel, (b) circuit for one electrode with the diffuse–double-layer capacitance, C_{ddl}, and diffusional capacitance, C_{diff}, substituted with constant phase elements (CPE_{ddl} and CPE_{diff}, respectively), and (c) circuit for a two-electrode experimental setup where the electrodes are assumed equivalent and the diffuse–double-layer is modeled as CPE_{ddl} and the sum of the charge-transfer and diffusion resistances are modeled at $R_{ct+diff}$.

Chapter 2 **Identification of Photoacidic Behavior Using Coupled AC and DC Electrochemical Techniques**

2.1. Introduction

Photoacids and photobases constitute a class of molecules where light absorption results in a reversible change in the Brønsted–Lowry acidity of a functional group on the molecule. Depending on the underlying mechanism of photoacidity/photobasicity, the cycle of light absorption, (de)protonation, and ultimate recombination/re-equilibration can occur over many different timescales that vary by 15 orders of magnitude.[55,57,69,92,93] For example, excited-state proton transfer (ESPT) from photoacids occurs on the timescale of picoseconds (nonadiabatic) up to nanoseconds (adiabatic), photobasic behavior often occurs on the timescale of up to microseconds,[61,94–96] regeneration of deprotonated ground-state photoacids occurs on the tens of milliseconds timescale,[62,97] and photo-driven cis/trans isomerization leading to cyclization and deprotonation, followed by re-equilibration, occurs on the timescale of seconds to minutes.[68,98,99] Because of these disparate timescales, techniques to measure photoacidic/photobasic behavior are quite varied. For slow non-excited-state proton-transfer processes such as cis/trans isomerization many rather facile techniques exist, including quantification of pH changes using a standard pH probe and electronic absorption spectroscopy to quantify the extent of (de)protonation and pH change.[99–103] Quantifying photoacidity/photobasicity of excited-state species requires faster time resolution, which is easily accessible using time-resolved photoluminescence spectroscopy even when the excited-state molecules are only weakly emissive.[104] However, when excited-state molecules are extremely poor light emitters, so much so that luminescence is undetectable experimentally, more advanced and less readily available techniques are required, such as ultrafast and nanosecond transient absorption spectroscopy. A

more easily accessible and generally applicable technique to identify photoacidic/photobasic behavior is useful.

Dawlaty et. al. recently demonstrated a photo-electrochemical impedance spectroscopy (PEIS) technique that quantitatively assessed whether a species in solution or in poly(ethylene glycol) was photoacidic.[83] The basis for the technique is that when photoacids are continuously illuminated there is a steady-state change in the concentration of solvated protons, which should result in a decrease in the series resistance of the bulk solution – measured at high frequencies – and a decrease in the impedance of mass-transport-limited processes involving protons at the electrodes – measured at low frequencies. Measuring changes in solution resistance is challenging because solution resistance is in series with other resistances, including charge transport in the plane of transparent-conductive-oxide electrodes whose resistances are often relatively large. Moreover, the ionic strength of the aqueous electrolytes used in these experiments is rather large due to water-solubilizing charged groups present on most photoacids and their mobile counterions. This means that changes in the series resistance during illumination will be small compared to the value of the series resistance in the dark, even with effective photoacids/photobases and moderate illumination intensities. Measuring changes in mass-transport-limited impedance is in theory less challenging because the measurement is specific to protons and hydroxides and therefore small and stable initial concentrations are possible, e.g. 10^{-7} M at pH 7. In order to observe a change in the mass-transport-limited resistance during illumination, protons and/or hydroxides must be involved in interfacial electron-transfer reactions at the electrode(s) and their concentration(s) must be perturbed significantly within the diffusion layer of an electrode(s). By illuminating an electrochemical cell whose walls consist

of transparent-conductive-oxide electrodes and that is filled with a solution of photoacids whose absorption profile follows the Beer–Lambert law, the largest number of excited states are generated at one electrode and therefore, as long as the potential of the electrode is sensitive to the local concentration of protons, a decrease in the low-frequency impedance should be observed upon illumination. Dawlaty et.al. demonstrated the utility of this technique using a well-known photoacid dye molecule (Sodium 8-hydroxypyrene-1,3,6-trisulfonate (HPTS); pyranine) dissolved in aqueous solution and impregnated into a hydrated polymer.[83] A general and somewhat initially unexpected conclusion was the charge-transfer resistance of the fitted photo-EIS data increased upon illumination. Herein we report data from dark and illuminated electrochemical measurements of aqueous pyranine solutions using open-circuit-potential measurements (DC) combined with photo-EIS measurements (AC). Together, the data provide a more complete picture of the processes that lead to the previously observed low-frequency photo-EIS response and further support that the response is due to a transient change in solvated proton activity.

2.2. Experimental Methods

2.2.1. Chemicals

The following materials were used without purification: hydrochloric acid (36.5 - 38.0% w/w, Fisher Scientific), sodium hydroxide (>95%, Macron Fine Chemicals), sodium chloride (99.6%, Fisher Scientific), Sodium 8-hydroxypyrene-1,3,6-trisulfonate (HPTS or pyranine) (>95%, Carbosmith), Iron(III) chloride, anhydrous (98%, Alfa Aesar), Iron(II) chloride, anhydrous (99%, Acros Organics). Sodium 8-methoxy-hydroxypyrene-1,3,6-trisulfonate (MPTS) was synthesized

using iodomethane (99%, Alfa Aesar) and sodium hydroxide (>95%, Macron Fine Chemicals) according to previously reported procedures.[105] Solutions were made using DI water unless otherwise noted.

2.2.2. Cell Design

Our cell was modeled after that used by Dawlaty et. Al.,[83] with several adjustments noted here, and was used to perform photo-electrochemical impedance spectroscopy **(**photo-EIS) measurements and electronic absorption spectroscopy measurements. Briefly, a thin-pathlength infrared (IR) spectroscopy liquid cell (Super-Sealed Liquid Cell, PIKE Technologies) was constructed using cell windows that consisted of electrically conductive optically transparent electrodes (fluorine-doped tin oxide-coated glass (FTO), Hartford Glass) separated by a 250 μm thick Teflon spacer. Electrical connections to the external circuit were made by contacting the top edge of each FTO with a copper wire via intervening silver paint and covered with epoxy. Two 3/16-inch holes, aligned with the injection ports of the IR cell, were drilled in one piece of FTO to allow for introduction of the photoacid-containing aqueous solutions. Prior to cell assembly, the electrodes were thoroughly cleaned with ethanol and acetone and dried under a stream of N_2(g). After cell assembly and compression by tightening the screws of the cell, 150μL of solution was injected to form a uniform layer, without air bubbles or separation, that was visible across the entire cell window.

2.2.3. Electronic Absorption Spectroscopy

Electronic absorption spectra were acquired at room temperature using an ultraviolet–visible absorption spectrophotometer (Cary 60, Agilent Technologies) with a resolution of 1 nm. Electronic absorption spectra were measured by aligning the window of the cell in the optical

beam path, and spectra are reported versus a baseline spectrum taken on the cell filled with Mill-Q and deionized water respective to the medium used as the solvent.

2.2.4. Photo-Electrochemical Impedance Spectroscopy (Photo-EIS).

The cell was aligned in a homebuilt Faraday cage that contained a small opening for cell illumination. Photo-EIS data were acquired from 0.1 to 10^6 Hz (4 points per decade and 10 mV AC voltage amplitude) in the dark and under constant illumination. Incident light was generated by a visible-light-emitting laser pointer (405 ± 10 nm) calibrated using a Si photodiode (FDS100, Thorlabs) to have a photon flux of 8.4 x 10^{15} photon s^{-1} and full-width-at-half-maximum beam diameter of 1.96 mm, followed by a beam expander that slightly undrilled the cell window to ensure near-complete illumination of the electrode over the area of the window.

2.2.5. Open Circuit Potential

The open circuit voltage (V_{OC}) was measured using the two-electrode cell in alternation with each photo-EIS measurement. Each open circuit potential measurement was measured for five seconds and recorded every second with a resolution potential range of -2.5 V; 2.5 V.

2.3. Results and Discussion.

Sodium 8-hydroxypyrene-1,3,6-trisulfonate (HPTS; pyranine) is a molecule that is known to undergo excited-state proton transfer when illuminated.[58,59,70,92,106] Excitation into its $\pi \rightarrow \pi^*$ absorption transition (Figure 2.1a) results in a decrease in its ground-state pK_a from ~7 to ~1 in the excited state.[59,104,105,107–109] Because this photoacid has been studied for decades, we used it as a model compound to demonstrate the utility of our coupled DC and AC photoelectrochemical techniques and assess the cause of the resulting photo-EIS behavior shown in Figure 2.2.

Shown in Figure 2.2 are Nyquist plots representations of photo-EIS data for aqueous solutions of 1 mM and 10 mM pyranine when fully protonated and fully deprotonated, as well as analogous data for methoxylated pyranine, which does not contain a protic proton. Comparative ultraviolet–visible electronic absorbance spectroscopy for each compound is shown in Figure 2.1.

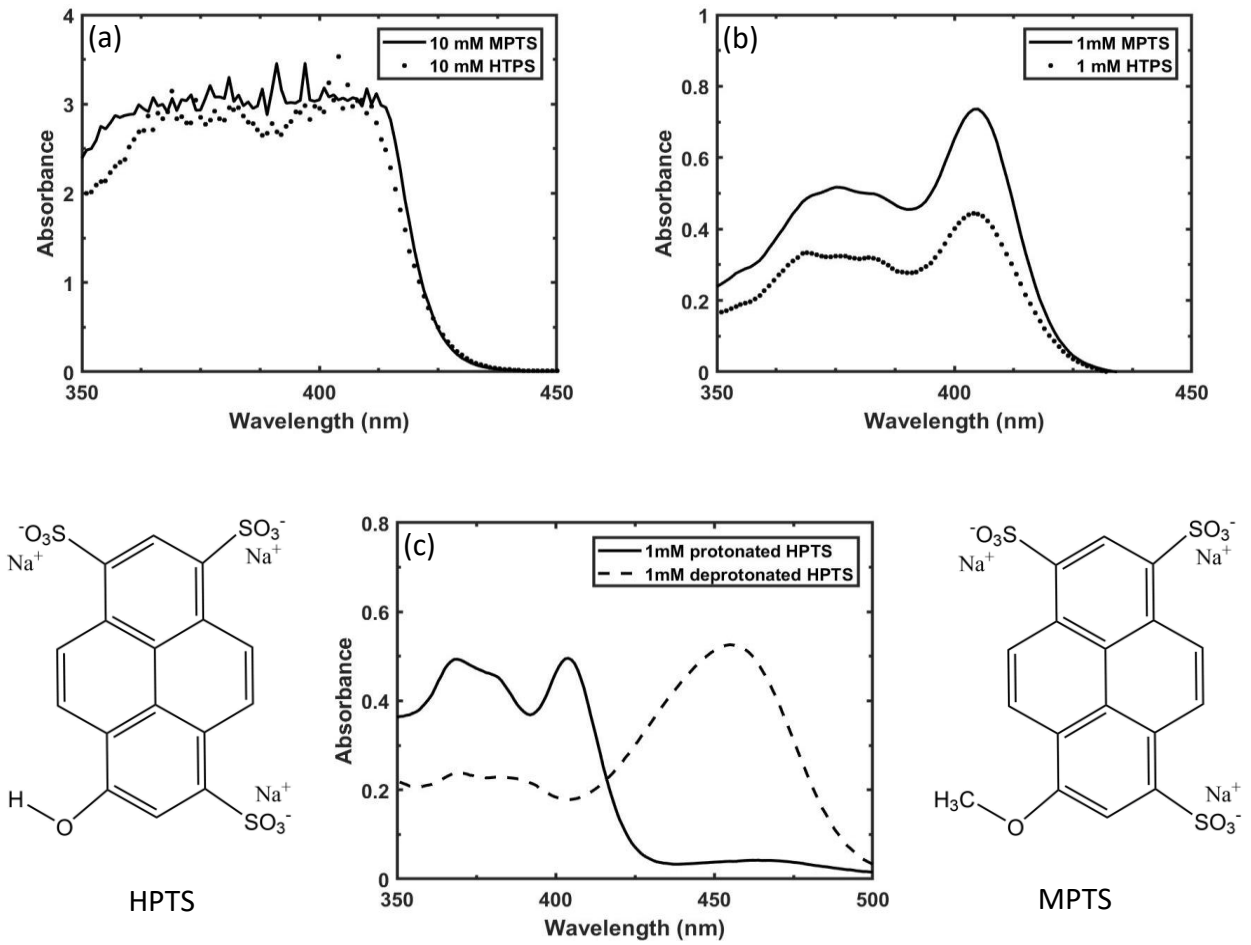

Figure 2.1 (a) Absorption of 10 mM protonated HPTS and 10 mM MPTS and (b) Absorption of 1 mM protonated HPTS and 1 mM MPTS, and c) 1 mM protonated HPTS and 1 mM deprotonated HPTS all with a pathlength of 250 µm

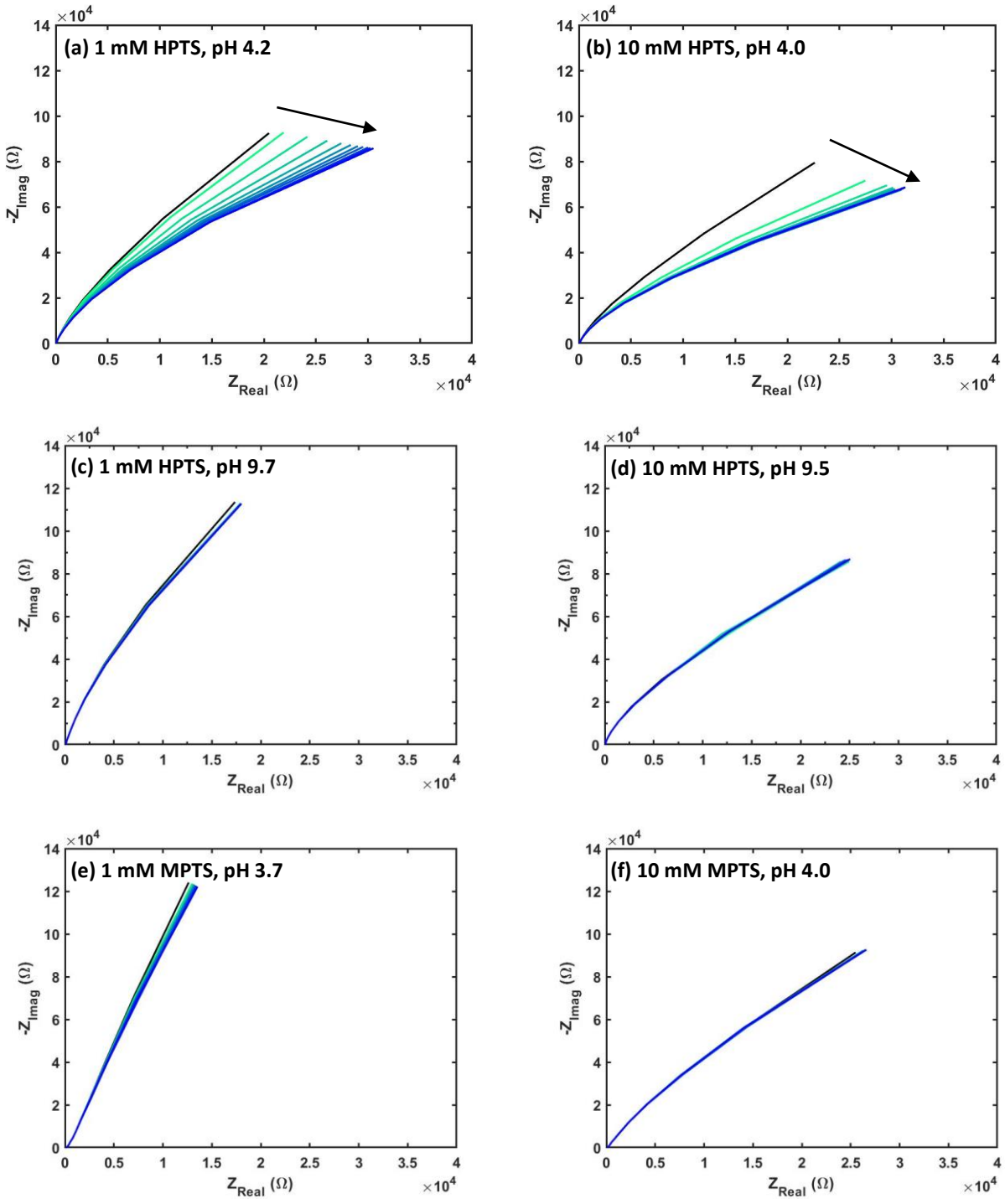

Figure 2.2. Time-dependent photo-EIS data plotted as Nyquist plots over time for aqueous solutions of 1 and 10 mM sodium salts of (a) 1 mM HPTS (pH 4.2), (b) 10 mM HPTS (pH 4.0) (c) 1 mM HPTS (pH 9.7 from addition of equimolar NaOH), (d) 10 mM HPTS (pH 9.5 from addition of equimolar NaOH), (e) 1 mM MPTS (pH 3.7), (f) 10 mM MPTS (pH 4.0), showing dark equilibrated photo-EIS spectra (black) and photo-EIS spectra measured successively over time until a maximum separation is observed under illumination (green-to-blue).

Collectively, these data clearly show that protonated ground-state pyranine is required in order to observe significant changes in the low-frequency region of the photo-EIS spectra under conditions of continuous illumination. The fact that deprotonated pyranine, at a different pH value, and methoxylated pyranine, at approximately the same pH value, did not exhibit significant light-induced changes in the photo-EIS spectra suggests that the protic proton on HPTS is important in order to observe this behavior and that the pH of the solution by itself does not strongly influence the effect. This is consistent with the behavior of protonated pyranine which undergoes excited-state proton transfer with near-unity quantum yield under these pH conditions.[110,111] Moreover, solutions containing other concentrations of protonated pyranine and at various other pH values also exhibited a similar change in photo-EIS spectra under conditions of continuous illumination (Figure 2.2). The trends in behavior observed here are consistent with observations made by Dawlaty et. al.,[83] and with a technique that is sensitive to the concentration of protons in solution.

A change in proton concentration under illumination can affect various aspects of an electrochemical cell: bulk resistance, diffuse-layer capacitance near the electrode|electrolyte interface, and mass-transport-limited proton-coupled redox reactivity at the electrode surface. Therefore, we performed a series of measurements to assess each of these processes.

Bulk resistance is inversely proportional to the ionic strength. Therefore, photo-generation of protons should result in a decrease in the bulk resistance as evidenced by a decrease in the value of the x-intercept of the Nyquist plot, which is measured at a high frequency. As illumination was toggled on and off the high-frequency photo-EIS data did not show a reproducible change in its shape or the value of the x-intercept, which suggests that light has little-to-no influence on the

bulk resistance of the cell. This observation occurred in part because for every molecule of pyranine, three Na^+ counterions were present, meaning that the ionic strength of the cell in the dark was inherently quite large and that small increases in proton concentration and therefore decreases in resistance would be difficult to measure. Moreover, the resistance of the FTO electrodes dominated the ohmic resistance of the circuit.

The diffuse-layer capacitance is directly related to the ionic strength and therefore, will be affected by the number of photo-generated protons; however, the double-layer capacitance is constant and therefore will not. Similarly, for measurements of the bulk resistance, the large ionic strength inherent to pyranine precludes significant changes in the capacitance of the diffuse layer. Moreover, the capacitance of the diffuse–double-layer is dominated by the smaller double-layer capacitance over most potentials and therefore, the observed capacitance will be relatively unaffected by photo-generated protons.

Mass-transport-limited proton-coupled redox reactivity at the electrode surface would result in a change in the low-frequency photo-EIS spectra, which was observed experimentally for photo-EIS data measured at < 1 Hz suggesting that during the ±10 mV AC sweeps, redox processes that consume or generate protons occur at the FTO electrode(s). This hypothesis was further corroborated by photo-EIS data measured in the presence of excess inert supporting electrolyte, which should not affect mass-transport-limited processes and did not (Figure 2.3). If mass-transport-limited proton-coupled redox reactivity at the electrode surface is the cause of the observed change in the photo-EIS spectra during illumination, then the open-circuit potential of the cell should also be affected by light.

Equimolar amounts were used in addition to 10x equimolar amounts to definitively show that the PEIS observations were not from an excess of electrolyte, also shown with open-circuit potential measurements (Figure 2.3(a)(b)). Unlike the case with added NaOH, these measurements exhibited a similar photo-EIS response in the presence and absence of NaCl suggesting that the magnitude of the photo-EIS signal is not due to a change in the ionic strength and/or conductivity of the solution, or a change in the rate of flux due to species migration under illumination, and is more likely reporting on a phenomenon that is specific to diffusion of protons/hydroxides. In the case of deprotonated photo-EIS measurements, an equimolar amount of NaOH and HPTS was used and an overall decrease in resistance was seen for both light and dark spectra. For the excess salt spectra, deviations from the photo-EIS spectra are not observed until 10x the amount of salt is added to a concentration of HPTS as shown in Figure 2.3(e). The small change in the high-frequency resistance with and without added NaCl, added in a 1:1 molar ratio to HPTS to match the 1:1 molar ratio of NaOH to HPTS further corroborates the hypothesis that the FTO electrode dominated the series resistance of the circuit.

Additionally, measurements were taken with both excess NaOH and HCl (20x the molar amount of HPTS) to see if the effect was similar to that of excess salt concentration (Figure(d)(e). For 20x the amount of HCl to HPTS, an overall decrease of resistance in both dark and light was seen which is similar to the case of 10x NaCl. However, for excess NaOH (20x molar amount of HPTS), although there was also a decrease in overall resistance similar to previous observations, the opposite effect was seen between dark and light spectra where the light spectra has a very small increase in resistance, possibly due to the heating of the sample. (Figure 2.3)

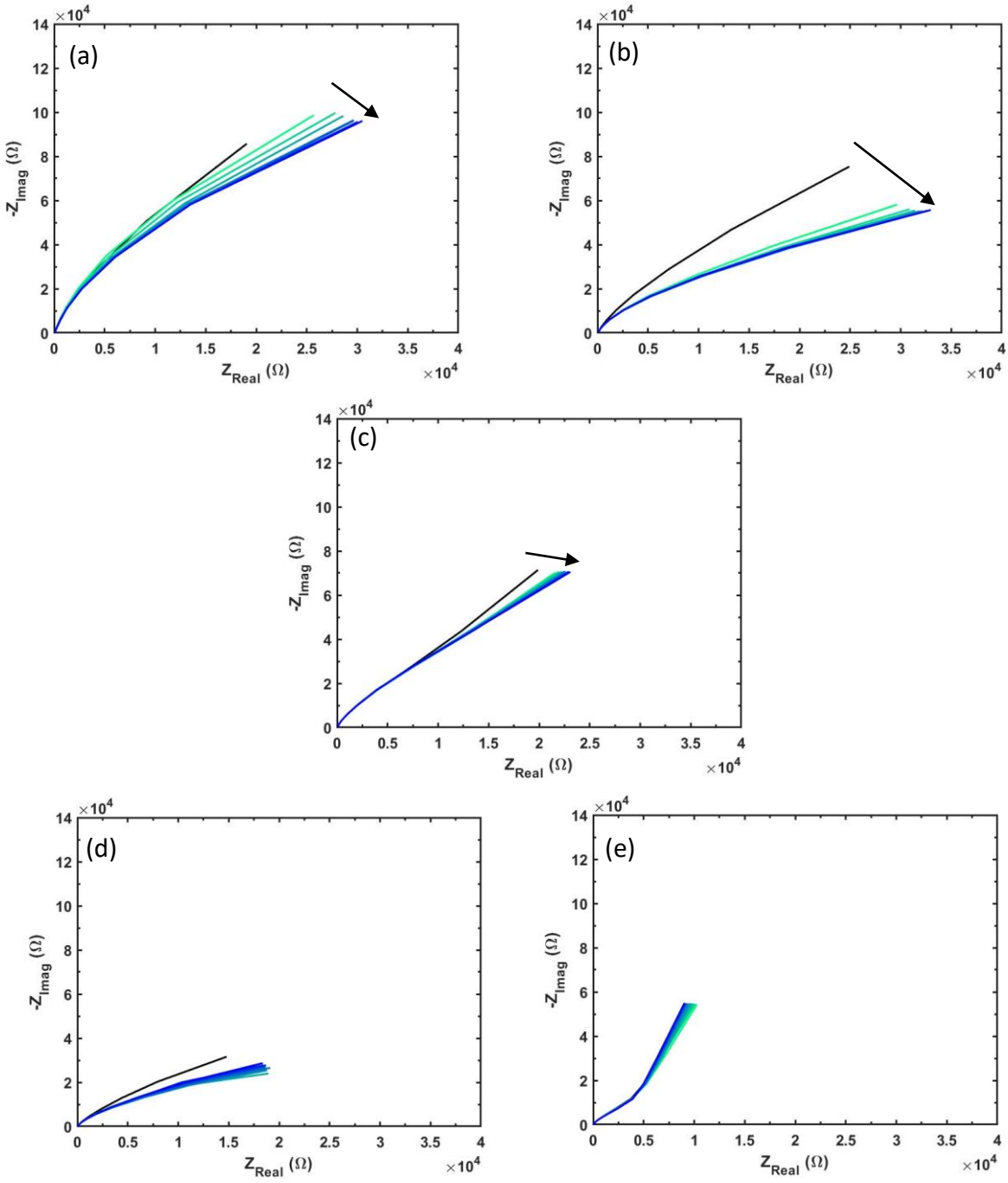

Figure 2.3 Time-dependent photo-EIS spectra (a) 1 mM HPTS and 1 mM NaCl (pH 4.25), (b) 10 mM HPTS and 10 mM NaCl (pH 4.27), and (c) 10 mM HPTS and 100 mM NaCl (pH 5.0), (d) 10 mM HPTS and 200 mM HCl (pH 0.89), and (e) 10 mM HPTS and 200 mM NaOH (pH 13.64) showing dark equilibrated photo-EIS spectra (black) and photo-EIS spectra measured successively over time until a maximum separation is observed under illumination (green-to-blue).

Lastly, the data provided in Figure 2.4 shows 1 mM and 10 mM HPTS solutions in Milli-Q water, which further confirms that observation of a decreased resistance for solutions of HPTS in the low-frequency region of the photo-EIS spectra are not due to impurities in the deionized water. The main difference is the trend of separation in the photo-EIS spectra: in deionized water the photo-EIS spectra further deviate from the dark photo-EIS spectra over successive measurements whereas with Milli-Q water the photo-EIS spectra immediately change to their largest deviation and then decrease back toward the dark photo-EIS spectra.

Therefore, we also examined the influence that light, concentration of pyranine, pH, and salt had on the open-circuit potential by performing DC galvanostatic open-circuit potential measurements over time. Unlike PEIS measurements that probe species distributions and dynamics across the entire cell, open-circuit potential measurements report only on phenomena

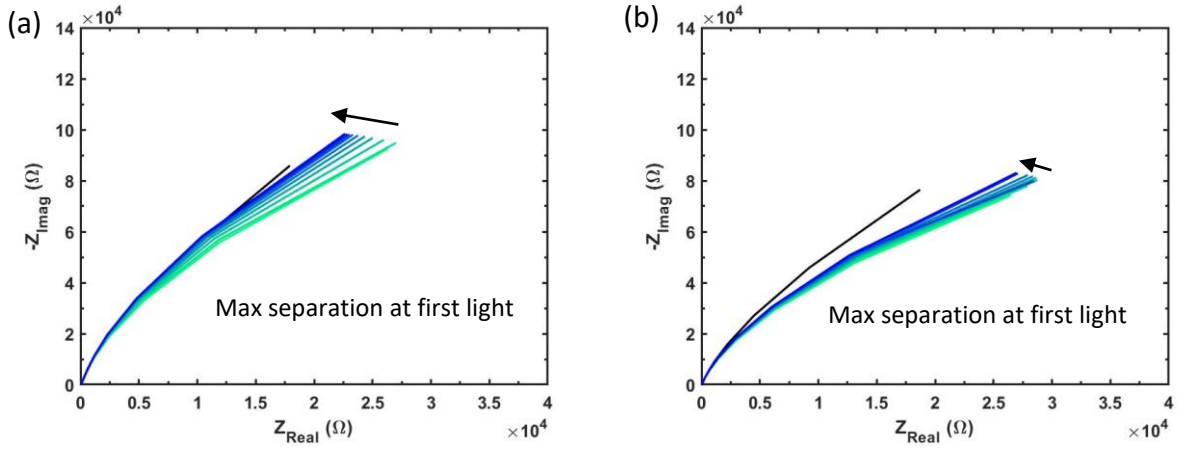

Figure 2.4 Time-dependent photo-EIS spectra (a) 1 mM HPTS in Milli-Q water at pH 4.24, and (b) 10 mM HPTS in Milli-Q water at pH 4.26 showing dark equilibrated EIS spectra (black) and photo-EIS spectra measured successively over time until a maximum separation is observed under illumination (green-to-blue).

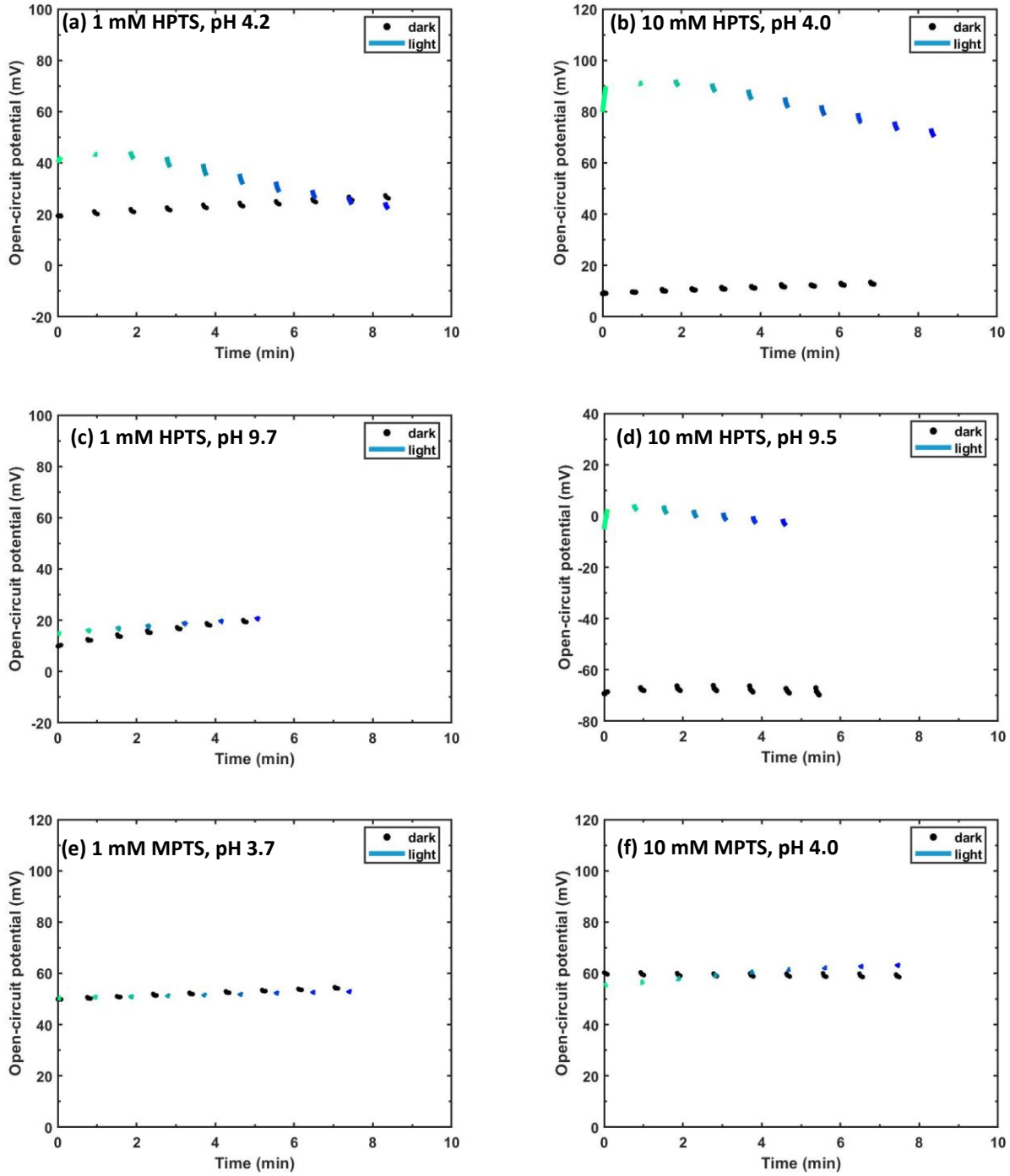

Figure 2.5 Open circuit potential data plotted over time taken in alternation with PEIS data in Figure 2.2 for aqueous solutions of 1 and 10 mM sodium salts of (a) 1 mM HPTS (pH 4.2), (b) 10 mM HPTS (pH 4.0) (c) 1 mM HPTS (pH 9.7 from addition of equimolar NaOH), (d) 10 mM HPTS (pH 9.5 from addition of equimolar NaOH), (e) 1 mM MPTS (pH 3.7), (f) 10 mM MPTS (pH 4.0), showing dark equilibrated EIS spectra (black) and photo-EIS spectra measured successively over time. Light is shown as a green to blue for increasing time corresponding to identical color EIS data

that result in local changes in species concentration at or near the electrode surface and any changes in the electric potential drop in the system.

The quasi-equilibrated open-circuit potential in the dark and the maximum open-circuit potential measured under conditions of continuous illumination are shown in Figure 2.5 for HPTS, deprotonated HPTS, and MPTS reported in Figure 2.2. These data are consistent with the hypothesis that photo-generated protons influence the potential of the electrode, which must have a pH dependence to its open-circuit potential and was confirmed (Figure 2.8). The trend can also be observed in the open-circuit photovoltage data in Figure 2.6 for excess electrolyte, 200 mM HCl, and 200 mM NaOH with HPTS reported in Figure 2.3. However, in the case of 10 mM HPTS and 200 mM NaOH, illumination results in a decrease in the open-circuit photovoltage, which differs from all other data. The changes are small, as expected for deprotonated HPTS, suggesting that the observed behavior may be due to local heating.

In the case of HPTS and Milli-Q water, the open-circuit photovoltage measurements reflect this faster change as compared to deionized water, which we collectively think may be due to a more well-defined potential present when deionized water is used from the larger concentrations of impurities in the water (Figure 2.7).

Similar behavior is observed when 1 μM Fe 3+/2+ redox couple is measured in Milli-Q water (Figure 2.9), which also exhibits pH-dependent redox reactivity. The slower observed rate of loss of the largest change in open-circuit photovoltage is likely due to the more well-defined potential formed at the electrode surface when a redox couple was intentionally added to the aqueous electrolyte solution resulting in less anomalous drift of the signal over time.

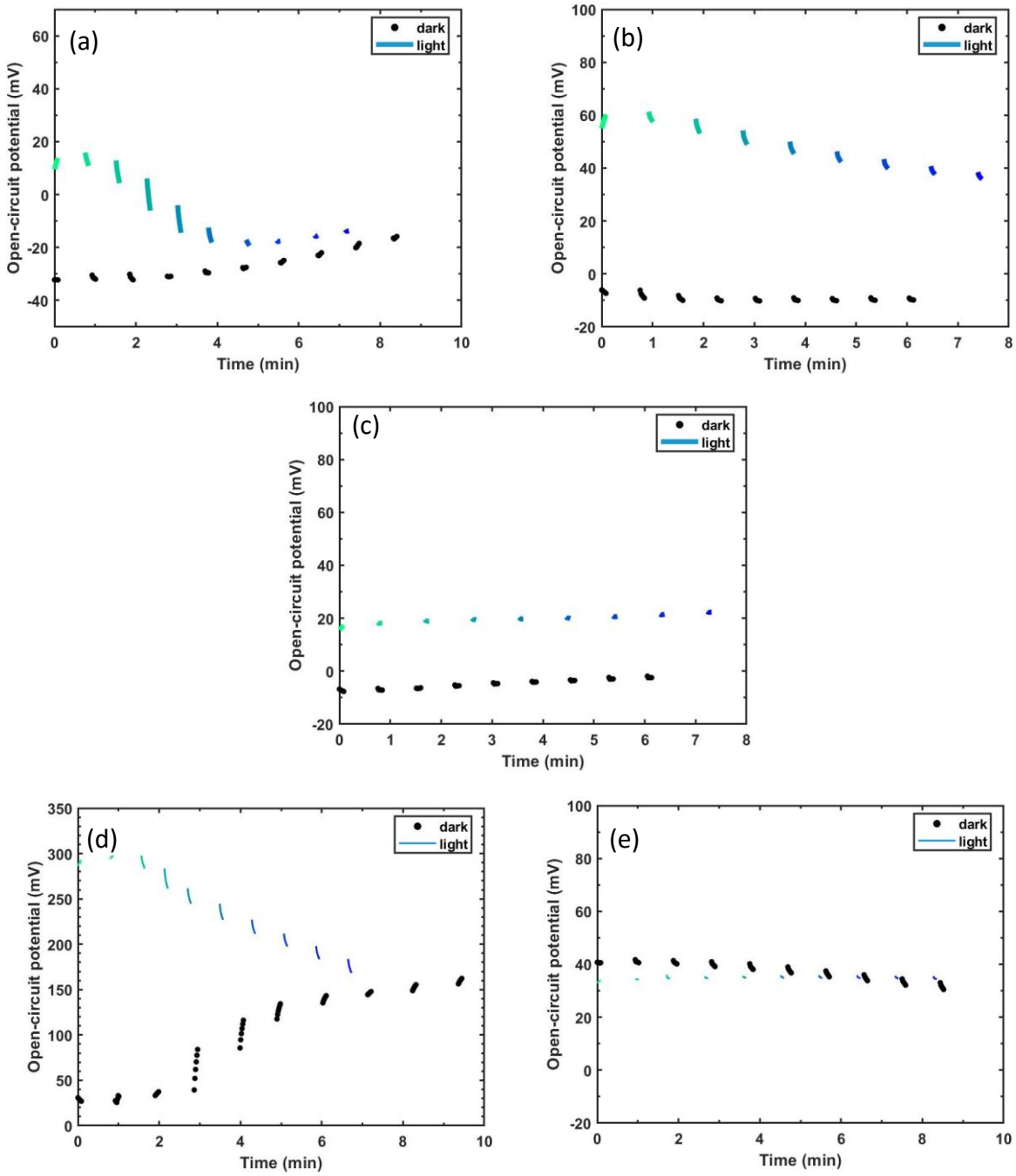

Figure 2.6 Open circuit potential data plotted over time taken in alternation with PEIS data in Figure 2.3 for aqueous solutions of 1 and 10 mM sodium salts of (a) 1 mM HPTS and 1 mM NaCl (pH 4.25), (b) 10 mM HPTS and 10 mM NaCl (pH 4.27), and (c) 10 mM HPTS and 100 mM NaCl at pH 5.0 (d) 10 mM HPTS and 200 mM HCl (pH 0.89), and (e) 10 mM HPTS and 200 mM NaOH (pH 13.64) showing V_{OC} spectra in dark (black) and under continuous illumination. Light is shown as a green to blue for increasing time corresponding to identical color EIS data

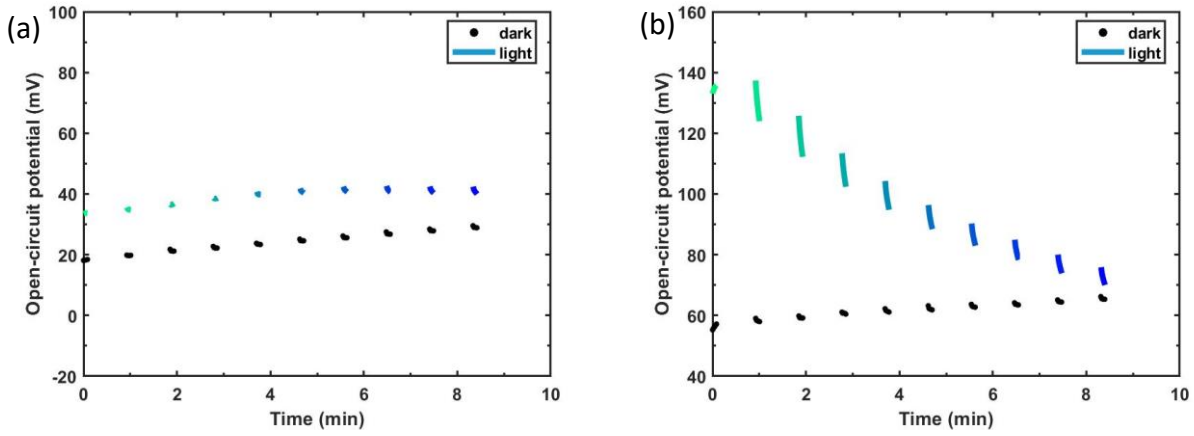

Figure 2.7 Open circuit potential data plotted over time taken in alternation with PEIS data in Figure 2.4 for aqueous solutions of 1 and 10 mM sodium salts of (a) 1 mM HPTS in Milli-Q water (pH 4.24) and (b) 10 mM HPTS in Milli-Q water (pH 4.26) showing V_{OC} spectra in dark (black) and under continuous illumination. Light is shown as a green to blue for increasing time corresponding to identical color EIS data.

All electrochemical measurements conducted under conditions of continuous illumination exhibited transient responses on the seconds-to-minutes timescale. This is consistent with the average time it takes for protons to diffuse across the width of the 250 µm thick cell, $\tau = \ell^2/D$ = $(0.025\ \text{cm})^2/(9.31 \times 10^{-5}\ \text{cm}^2/\text{s}) \approx 10$ sec. The initial time dependence of the photo-EIS and open-circuit photovoltage data were remarkably similar (Figures 2.2 and 2.4). As the photovoltage increased in magnitude, the photo-EIS data exhibited a similar decrease in slope.

However, the magnitude of the open-circuit photovoltage quickly decreased toward values measured in the dark, while the photo-EIS data remained rather constant. Moreover, when the direction of illumination was switched, the sign of the photovoltage changed yet the photo-EIS response was similar, further indicating that the electrodes exhibit a pH-dependent open-circuit potential that is influenced by protons that are photo-liberated from protonated pyranine close to the electrode surface.

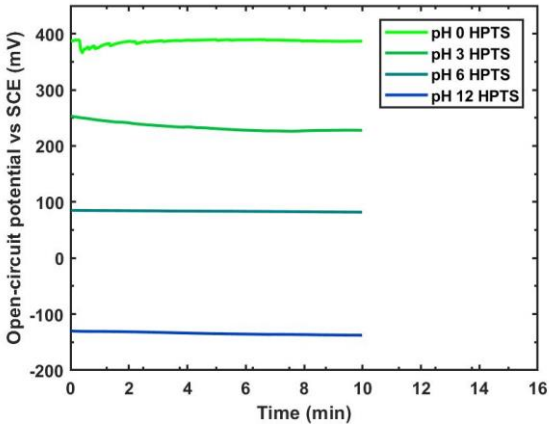

Figure 2.8 pH dependence of the open-circuit potential of FTO in contact with an aqueous electrolyte solution containing HPTS.

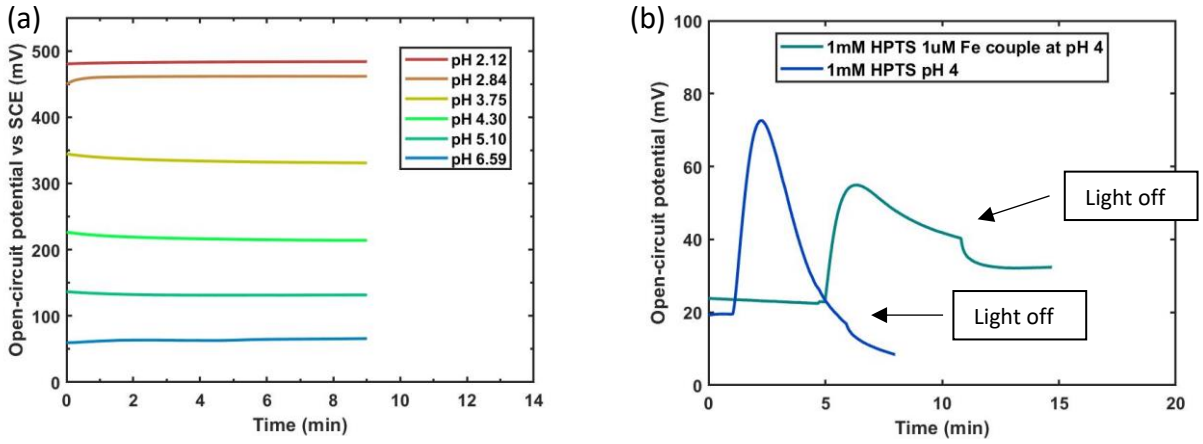

Figure 2.9 (a) pH dependence of the open-circuit potential of FTO in contact with an aqueous electrolyte solution containing 1 µM Fe 3+/2+ redox couple in Milli-Q water (b) Open-circuit potential comparison between aqueous electrolyte solutions at pH 4 containing 1 mM HPTS, with and without 1 µM Fe 3+/2+ redox couple.

Unlike the open-circuit potential data, at all times the photo-EIS data is a convolution of effects at both electrodes and should not exhibit much of a polarity dependence, where a decrease in the slope of the low-frequency photo-EIS data suggests that more protons are present near either electrode. Because the open-circuit potential data is electrode specific and two-electrode measurements were performed, one would expect that under illumination diffusion of protons occurs across the cell on the seconds-to-minutes timescale and over which time the photovoltage measured as a difference in potential between the two electrodes would approach zero; this was observed experimentally.

Collectively, the data are consistent with photo-generated protons affecting the pH-dependent potential of the electrode. However, in order to more clearly understand the change in the low-frequency impedance under illumination, where mass-transport diffusional Warburg impedance dominates,[84–86,112] we performed further analyses of the photo-EIS spectra. Warburg impedance is based on a simple linear diffusion model that follows Fick's laws of diffusion and exhibits a characteristic trend as a function of the logarithm of the frequency in both the logarithm of the magnitude of the impedance, $|Z|$, of -1/2 and current and potential that are 45° out-of-phase. Both of these effects are more easily visualized in Bode plots (Figure 2.10), which present the change in magnitude of impedance and the phase shift of the voltage/current relationship with respect to the frequency. The data clearly show trends for slope in $|Z|$ of -1 with current and potential that are -90° out-of-phase, which is not consistent with a Warburg impedance and is instead consistent with purely capacitive behavior. Thus, either the low-frequency response is due to interfacial capacitance near the electrode|electrolyte interface or that the diffusional process is more akin to a capacitor. At the 0.1 Hz frequencies analyzed,

species are able to diffuse between the electrodes suggesting that the diffusion process is limited by the counter electrode and thus is not semi-infinite as required for derivation of purely Warburg diffusion. Limited/confined diffusion can be modeled at low frequencies by replacing the Warburg element with a parallel RC circuit, where R stands for the diffusional mass-transport resistance and C stands for the capacitance of the boundary that limits diffusion. Because the boundary that limits diffusion is the counter electrode and two-electrode measurements are performed, which report on behavior at both electrodes at all frequencies, the capacitor representing the counter electrode is included in the capacitive element of the diffuse–double-layer from the outset. Therefore, when the diffusion layer reaches the counter electrode, no additional interfacial capacitance is introduced, and thus a Warburg impedance can be represented by a resistor at low frequencies and under our experimental conditions.

In all cases the slope of the logarithm of |Z| magnitude versus the logarithm of frequency in the Bode plot is closer to -1 rather than -1/2 and the phase change approaches -90° which shows that either there is a large deviation from ideal Warburg diffusion or that it's a different diffusion system entirely, which could be hypothesized to be a finite or anomalous diffusion with an absorbing finite boundary rather than an infinite. Using this information, the circuit model where the diffusive Warburg element in the Randles circuit, has been replaced by a parallel RC circuit element. The double layer and parallel diffusion capacitances are substituted for constant phase elements, representing deviation from ideal capacitance of the system.

Furthermore, in two-electrode electrochemical measurements both electrodes are being polarized and influenced at all frequencies and thus at low frequencies when the diffusion layer reaches the other electrode, no additional interfacial capacitance is being introduced.

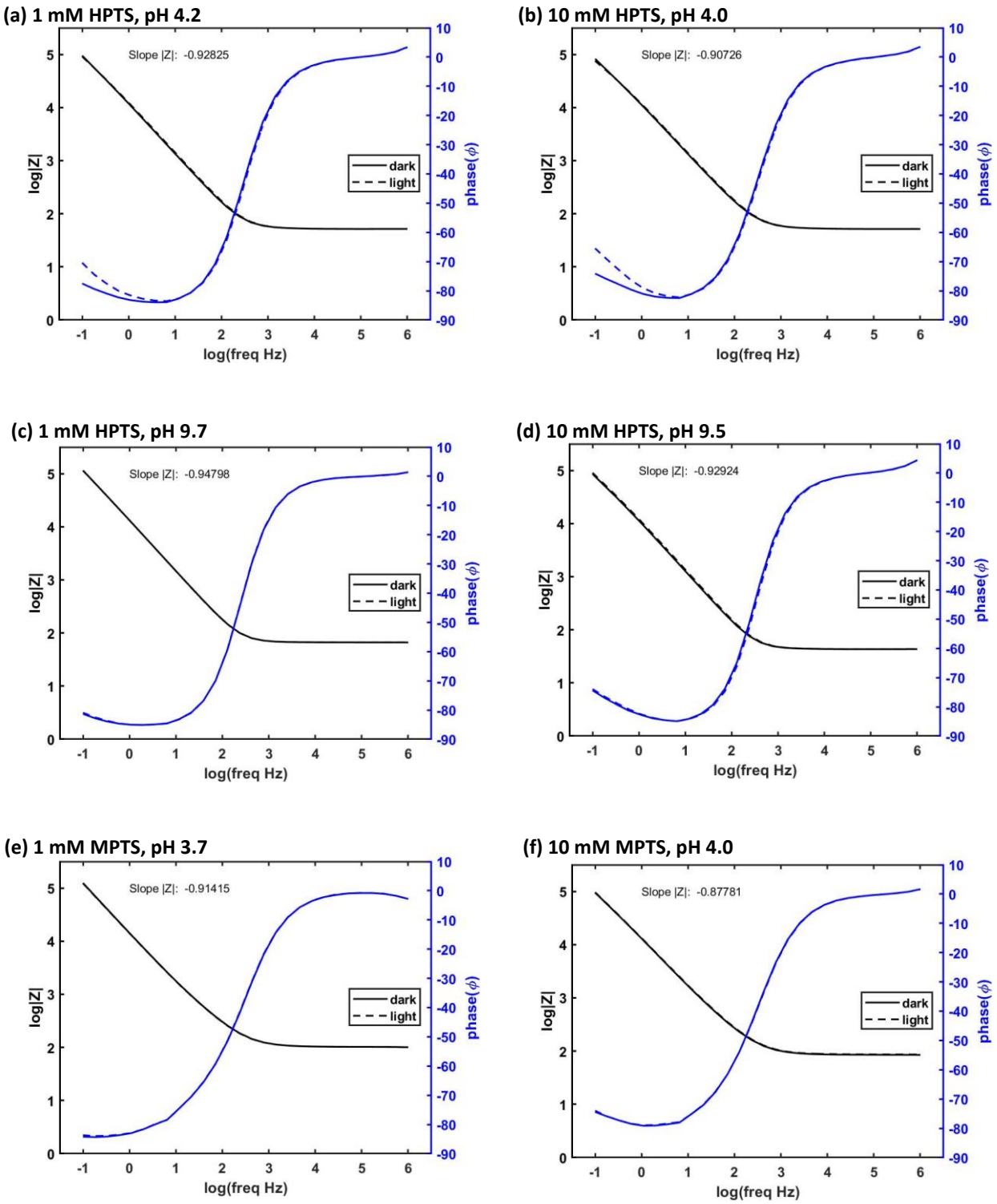

Figure 2.10 Bode plots of dark and max light spectra from Nyquist plot of aqueous solutions of 1 and 10 mM sodium salts of (a) 1 mM HPTS (pH 4.2), (b) 10 mM HPTS (pH 4.0) (c) 1 mM HPTS(pH 9.7 from addition of equimolar NaOH), (d) 10 mM HPTS (pH 9.5 from addition of equimolar NaOH), (e) 1 mM MPTS (pH 3.7), (f) 10 mM MPTS (pH 4.0) All data showing |Z| slope close to -1 and phase shift of or close to -90°

Combining the parallel diffusion constant phase elements in the equivalent circuit diagram leaves two resistors in series, R_{ct} and R_{diff}, which add together to form the total charge transfer and mass transfer diffusional resistance. The final simplified circuit model is shown in Figure 2.11, where a constant phase element is used for the diffuse–double-layer capacitance to represent slightly non-ideal capacitive behavior. The fits from the model are shown in Figure 2.9 with additional data provided in Table 2.1. The fits were done using EC-LAB Version 11.27 impedance fitting software from Bio-Logic Science Instruments (Method: Levenberg–Marquard, Weight: |Z|, and 5000 iterations). Both light and dark data were simulated using the circuit model shown in Figure 2.11b and data was tabulated as shown in Table 2.1. The values for solution resistance, R_s, are taken from the real axis of the Nyquist plot at the intersection of the x-axis. The values for the constant phase element, C_{dl}, and the ideality factor were averaged for data in the light and the dark because the values only differed by 0.8-1.5%.

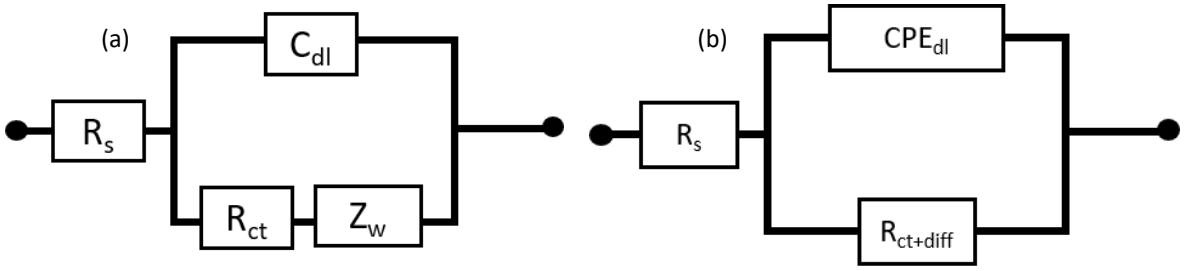

Figure 2.11 (a) Randles equivalent circuit where R_s represents the electrolyte resistance, the parallel capacitance, C_{ddl} represents the capacitance of the diffuse–double-layer, R_{ct} relates to the charge-transfer resistance at the surface of the electrodes, and the Warburg element, Z_w, represents the diffusion impedance and (b) The simplified model used where Z_w has been replaced by a parallel RC (R_{diff}/C_{diff}) circuit representing diffusion. R_s represents the electrolyte resistance, the parallel capacitance, C_{ddl} is replaced with a constant phase element relating to an imperfect capacitor and combined with the parallel C_{diff} represented in the Warburg element, Z_w, and the R_{ct} is combined with the series resistor element of the Warburg impedance, R_{diff}, and replaced with a resistor combining the charge transfer and the diffusion in the system, $R_{ct + diff}$.

These average values were then used to remodel both light and dark spectra to study the deviation in mass-transport resistance and charge-transfer resistance between dark and light. In both 1 mM and 10 mM HPTS a 55% decrease in resistance is seen upon illumination.

The final values are shown in Table 2.2. The trends in the data are as expected in that under illumination the sum of the charge-transfer resistance and the mass transport resistance decrease. We think that the main contributor to this effect is mass transport because charge-transfer reactions are likely facile at FTO. Moreover, experiments that included 1 µM Fe 3+/2+ redox couple in Milli-Q water exhibited a similar effect where charge-transfer resistance would have been very small (Figure 2.9).

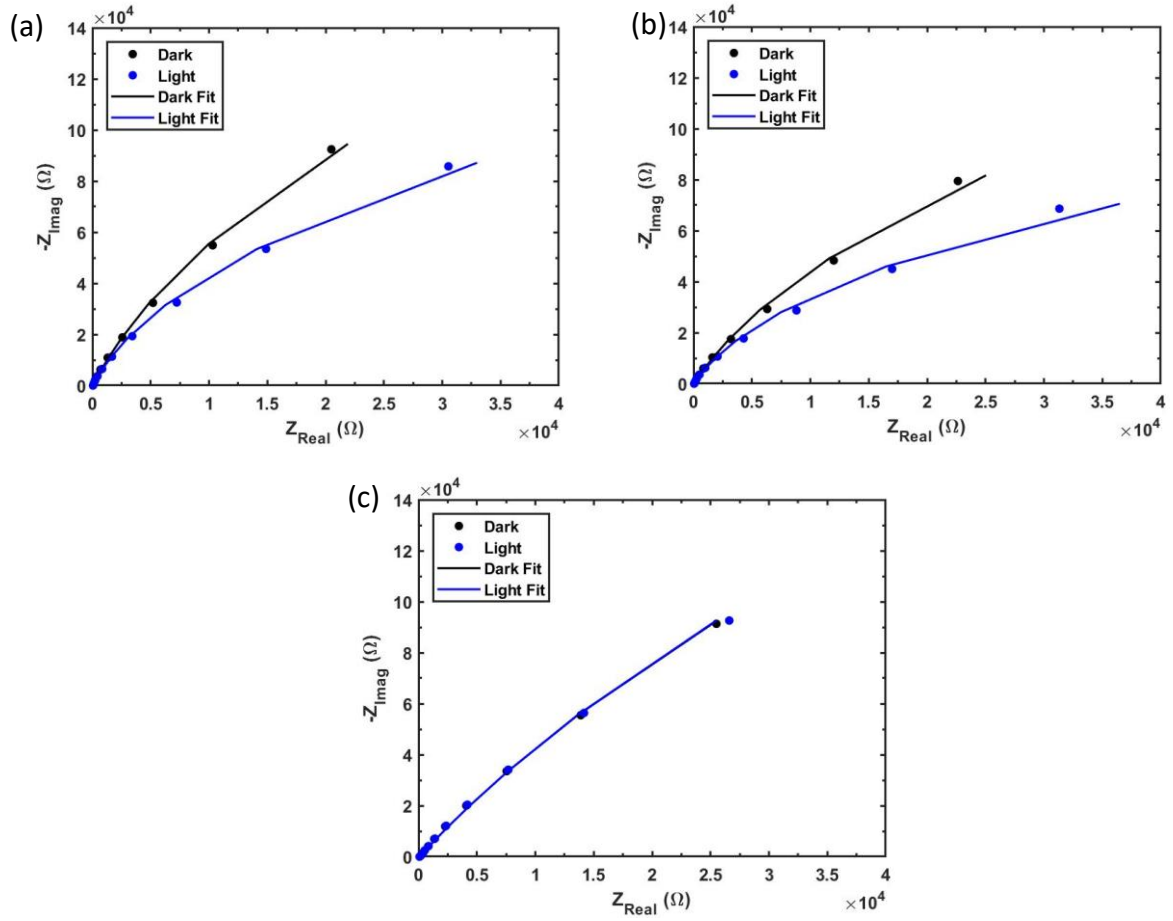

Figure 2.12 Fits of photo-EIS data using EC-Lab Zfit by Biologic for (a) 1 mM HPTS, pH 4.2, (b) 10 mM HPTS, pH 4.0, (c) 10 mM MPTS, pH 4.0.

Table 2.1 Data obtained for photo-EIS data using EC-Lab Zfit by Bio-Logic for HPTS and MPTS. All components were varied except for the values for solution resistance, R_s, taken from the real axis of the Nyquist plot at the intersection of the x-axis.

Material	Circuit Element	Units	Dark	Deviation	Light	Deviation
1 mM HPTS	R_s	Ω	51.7	x-int	51.8	x-int
	CPE_{dl}	$F•s^{(a-1)}$	15.62e-6	.8978e-9	15.5e-6	1.117e-9
	a_{dl}		.9344	.5002	.9279	.5002
	$R_{ct+diff}$	Ω	794774	620.7	293889	146.2
Material	**Circuit Element**	**Units**	**Dark**	**Deviation**	**Light**	**Deviation**
10 mM HPTS	R_s	Ω	51.7	x-int	51.7	x-int
	CPE_{dl}	$F•s^{(a-1)}$	17.38e-6	1.34e-9	17.13e-6	1.598e-9
	a_{dl}		.9151	.5002	.9103	.5001
	$R_{ct+diff}$	Ω	548863	346.5	265735	67.88
Material	**Circuit Element**	**Units**	**Dark**	**Deviation**	**Light**	**Deviation**
10 mM MPTS	R_s	Ω	85.4	x-int	86.9	x-int
	CPE_{dl}	$F•s^{(a-1)}$	15.51e-6	1.146e-9	15.27e-6	1.126e-9
	a_{dl}		.8763	.5001	.8738	.5001
	$R_{ct+diff}$	Ω	1.253e6	1353	1.238e6	1269

Table 2.2 The values for solution resistance, R_s, are taken from the real axis of the Nyquist plot at the intersection of the x-axis. The values for the constant phase element, C_{dl}, and the ideality factor were averaged for both and used to remodel both light and dark spectra with constant values to study the deviation of resistance between dark and light measurements.

Material	Circuit Element	Units	Dark	Deviation	Light	Deviation
1 mM HPTS	R_s	Ω	51.7	x-int	51.8	x-int
	CPE_{dl}	$F•s^{(a-1)}$	15.56e-6		15.56e-6	
	a_{dl}		.9312		.9312	
	$R_{ct+diff}$	Ω	812428	.01205	370124	.02845
Material	**Circuit Element**	**Units**	**Dark**	**Deviation**	**Light**	**Deviation**
10 mM HPTS	R_s	Ω	51.7	x-int	51.7	x-int
	CPE_{dl}	$F•s^{(a-1)}$	17.26e-6		17.26e-6	
	a_{dl}		.9127		.9127	
	$R_{ct+diff}$	Ω	532810	.01744	236290	.06075
Material	**Circuit Element**	**Units**	**Dark**	**Deviation**	**Light**	**Deviation**
10 mM MPTS	R_s	Ω	85.4	x-int	86.9	x-int
	CPE_{dl}	$F•s^{(a-1)}$	15.39e-6		15.39e-6	
	a_{dl}		.8751		.8751	
	$R_{ct+diff}$	Ω	1.306e6	4.02e-3	1.319e6	3.978e-3

2.4. Conclusions

The photoacidity of a well-known photoacid, 8-hydroxypyrene-1,3,6-trisulfonic acid trisodium salt (HPTS; pyranine), was successfully measured using electrochemical impedance spectroscopy. The electrochemical impedance spectra showed a significant decrease in resistance between measurements performed in the dark and under illumination for various concentrations of HPTS. Control measurements were performed using methoxylated HPTS, sodium 8-methoxy-hydroxypyrene-1,3,6-trisulfonate (MPTS) and deprotonated HPTS to ensure the change in photo-EIS spectra were due to changes in the concentration of protons and not due to an artifact. These controls measurements showed no change between measurements performed in the dark and under illumination. In addition, to support a change in the concentration of protons under illumination was not manifest by a change in the ohmic resistance in the cell, excess NaCl and excess HCl were added to the electrolyte and a change in low-frequency resistance between measurements performed in the dark and under illumination was still observed, with no noticeable change in the high-frequency resistance. Additionally, Mill-Q water was used to ensure that deionized water was not having an unexpected effect on the change observed in photo-EIS spectra with HPTS and showed a significant difference under illumination. The only significant difference between samples using Milli-Q water and deionized water was that the photo-EIS spectra under illumination with deionized water gradually grew into a maximum change in low-frequency resistance and was static whereas the Milli-Q samples featured an immediate growth and decay possibly due to the reduction of free ions in the solvent. Alternating open-circuit potential measurements between photo-EIS measurements was an

additional confirmation that there was a diffusion difference between electrodes upon illumination.

Chapter 3 **Demonstration of Photoacidic Quantum Dots**

3.1. Introduction

Photoacids are a class of molecules and polymers that exhibit a light-driven change in the energetics of a protic bond so that a proton is energetically more likely to be dissociated in the excited-state than in the ground-state.[62,97,111] Their photochemical cycle for photo-induced proton transfer consists of light absorption, proton transfer, relaxation to their ground states, and reprotonation of their conjugate base form was first described by Grabowski and Förster in the 1970s.[62,111] The first experimental demonstration of a photoacid was reported in 1931 by Weber using fluorescence spectroscopy and so have been studied for over half a century.[61,68,69,92,107,113,114] Several classes of photoacids exist, including those that undergo one or several rounds of adiabatic excited-state deprotonation and reprotonation reactions to reach a quasi-thermal equilibrium in their excited state, and termed excited-state proton transfer, and those that undergo nonadiabatic reactions where deprotonation results in prompt/concerted deactivation of the excited state.[61,94–96] The properties of the former class of adiabatic photoacids are easily quantified via a pH titration with detection by absorption spectroscopy and time-resolved and steady-state photoluminescence spectroscopy.[59,61,104,115] Notably, in either case the deprotonation reaction is reversible in that the ground-state of the photoacid can be regenerated via a reprotonation reaction, which is analogous to a typical excited-state electron-transfer dye sensitizer that can be regenerated by electron transfer. This trait sets this class of photoacid molecules apart from photoacid generators used in photolithography, which undergo irreversible proton transfer and cannot be used for photochemical energy conversion and net energy storage.[116] Moreover, analogous molecules and polymers exist that are classified as photobases and photobase generators, which undergo analogous reactions as their photoacid analogs by

either deprotonating a water or hydronium molecule[117,118] or releasing a hydroxide[119–121] after absorbing a photon.

Dawlaty et. al. recently demonstrated an electrochemical impedance spectroscopy technique that qualitatively assessed whether a species in solution or in a hydrogel was photoacidic.[83] The basis for the technique was that when photoacids are illuminated with steady-state irradiation there is a change in the concentration of solvated protons, which should result in a decrease in the resistance of the bulk solution and a decrease in the resistance of mass-transport-limited processes at the electrode.[122] Measuring decreases in solution resistance via changes in the magnitude of the high-frequency impedance of the circuit is challenging because photoacids are often highly charged molecules in order to increase their water solubility and attenuate their aggregation. Surface-confined uncharged photoacids have not been previously studied. Measuring decreases in mass-transport-limited resistance via changes in the magnitude of the low-frequency impedance of the circuit is less challenging. However, this requires that the concentration of species involved in the interfacial electron-transfer reactions on that low-frequency timescale are perturbed significantly within the diffusion layer from an electrode. By illuminating a transparent thin-pathlength electrochemical cell filled with a solution of photoacids whose absorption profile follows the Beer–Lambert law, the largest number of excited states are generated at one electrode and therefore, *as long as the electrode is sensitive to the local concentration of protons*, a decrease in the low-frequency impedance should be observed. Dawlaty and colleagues demonstrated the utility of this technique using a well-known photoacid dye molecule, pyranine, dissolved in aqueous solution and dissolved in a hydrogel.

Recently, photoacids have been utilized in a new class of solar-energy conversion devices where light absorption by photoacids results in power generation through ion transport.[106] This solar-energy conversion process is uniquely suited for application in a device for direct desalination of salt water.[123] The (protonic) semiconducting medium of these photovoltaic devices is water, and assuming that water in these materials has the same properties as bulk water, significant light absorption must occur over a very thin region in order for photogenerated mobile protons (and/or hydroxides) to be effectively charge separated and collected, due to their short collection lengths.[124] Because the rate of desalination is ultimately dictated by the rate of photogenerated charge separation, photoacids must also absorb visible light strongly. These conditions limit the choice of photoacids to only those with extremely large molar absorptivities and broad spectral coverage, such as quantum dots, porphyrins, and related chromophores, each with molar absorptivities on the order of $10^5 – 10^7$ M^{-1} cm^{-1}.[125–127]

Motivated by the aforementioned information we set out to synthesize the first quantum dot photoacid and demonstrate excited-state proton transfer, specifically through binding acidic functional groups to CdSe quantum dot surfaces. We leveraged prior knowledge on II–VI quantum dots to synthesize strongly absorbing quantum dots and used strategies imparted in model photoacids, such as pyranine, to impart photoacidity. This includes the presence of many water-solubilizing charged groups with extremely small pK_a values, such as sulfonates, to maintain a charged surface over a broad range of pH values. This also includes the presence of fewer protic groups with moderate pK_a values, such as benzylic alcohols, to serve as groups with pK_a values that can change upon photoexcitation. This also allows for photo-generation of a state with a much larger dipole than in the ground-state via loss of electron density near the protic

functional group, such as photoinduced charge-transfer states in donor–acceptor molecules, to enable effective and large photoacidity. Therefore, through judicious choice of synthesis and ligand exchange conditions we introduced water-solubilizing 2-mercaptoethanesulfonate (MES) ligands and a smaller concentration of protic and dipolar 4-mercaptophenol (MPh) groups. The energetics of surface-bound MPh groups are such that they can serve as electron-transfer donors to excited-state CdSe quantum dots. This is supported by transient absorption data taken after pulsed-laser excitation of CdSe thin films with MPh capping ligands deposited using SILAR on TiO_2 that were consistent with a reduced nanocrystal and an oxidized 4-mercaptophenol ligand.[73,128] The challenge to characterize the photoacidity of this class of chromophores is that this charge-transfer state does not efficiently emit photons as the photophysical properties of CdSe QDs are often affected by the addition of thiol capping ligands, particularly with MPh where the photoluminescence is quenched.[128] Moreover, pH titration of these proposed quantum dot photoacids resulted in few spectral changes that could clearly be ascribed to deprotonation events at the 4-mercaptophenol ligands and/or degradation due to ligand loss due to the instability of the quantum dots in extreme pH conditions.[76,77] Because these spectra would also serve as standard spectra for accurate identification of species formed transiently after photoexcitation, this also precluded quantitative assessment of spectroscopic data obtained using ultrafast transient absorption spectroscopy. Therefore, we utilized the recently developed electrochemical impedance spectroscopy technique to definitively demonstrate that our new class of quantum dot dyes were photoacidic. This represents the first demonstration of a quantum dot photoacid.

3.2. Experimental Methods

3.2.1. Materials

Cadmium oxide (CdO, ≥99.99%), oleic acid (OA, tech. grade, 90%), 1-octadecene (ODE, tech. grade, 90%), selenium powder (99.99%), chloroform (anhydrous, 99+%), hexane (95%), and ethanol (≥99.5%) were purchased from Aldrich. 3-mercaptopropionic acid (MPA), 4-mercaptophenol (MPh), and 2-mercaptoethanesulfonate (MES) All chemicals were used as received.

3.2.2. Electrochemical Impedance Spectroscopy

Our cell was modeled after that used by Dawlaty et. Al.,[83] with several adjustments noted here, and was used to perform photo-electrochemical impedance spectroscopy **(**photo-EIS) measurements and electronic absorption spectroscopy measurements. Briefly, a thin-pathlength infrared (IR) spectroscopy liquid cell (Super-Sealed Liquid Cell, PIKE Technologies) was constructed using cell windows that consisted of electrically conductive optically transparent electrodes (fluorine-doped tin oxide-coated glass (FTO), Hartford Glass) separated by a 250 μm thick Teflon spacer. Electrical connections to the external circuit were made by contacting the top edge of each FTO with a copper wire via intervening silver paint and covered with epoxy. Two 3/16-inch holes, aligned with the injection ports of the IR cell, were drilled in one piece of FTO to allow for introduction of the photoacid-containing aqueous solutions. Prior to cell assembly, the electrodes were thoroughly cleaned with ethanol and acetone and dried under a stream of N_2(g). After cell assembly and compression by tightening the screws of the cell, 150μL of solution was

injected to form a uniform layer, without air bubbles or separation, that was visible across the entire cell window.

3.2.3. Electronic Absorption Spectroscopy

Electronic absorption spectra were acquired at room temperature using an ultraviolet–visible absorption spectrophotometer (Cary 60, Agilent Technologies) with a resolution of 1 nm. Electronic absorption spectra were measured by aligning the window of the cell in the optical beam path, and spectra are reported versus a baseline spectrum taken on the cell filled with Mill-Q and deionized water respective to the medium used as the solvent.

3.2.4. Photo-Electrochemical Impedance Spectroscopy (Photo-EIS).

The cell was aligned in a homebuilt Faraday cage that contained a small opening for cell illumination. photo-EIS data were acquired from 0.1 to 10^6 Hz (4 points per decade and 10 mV AC voltage amplitude) in the dark and under constant illumination. Incident light was generated by a visible-light-emitting laser pointer (405 ± 10 nm) calibrated using a Si photodiode (FDS100, Thorlabs) to have a photon flux of 8.4 x 10^{15} photon s^{-1} and full-width-at-half-maximum beam diameter of 1.96 mm, followed by a beam expander that slightly undrilled the cell window to ensure near-complete illumination of the electrode over the area of the window.

3.2.5. Open Circuit Potential

The open circuit voltage (V_{OC}) was measured using the two-electrode cell in alternation with each photo-EIS measurement. Each open circuit potential measurement was measured for five seconds and recorded every second with a resolution potential range of -2.5 V; 2.5 V.

3.2.6. X-Ray Diffraction

Grazing-incidence X-ray diffraction (GIXRD) data were collected using a Rigaku Smartlab diffractometer with Cu Kα radiation and in parallel-beam geometry.

3.2.7. Fourier Transform Infrared Spectroscopy

Fourier-transform infrared spectroscopy in attenuated total reflectance (ATR) detection mode was performed on a Jasco FT/IR-4700 spectrophotometer equipped with a monolithic diamond ATR crystal. Spectra were acquired with a resolution of 1 cm^{-1} and an acquisition time of 74 s, and spectra are reported versus a baseline spectrum taken on methanol for all ligand exchanged quantum dots and chloroform for CdSe-oleate.

3.2.8. CdSe Nanocrystal Synthesis

CdSe quantum dots were synthesized following a previously reported method with some modifications.[80] A 50 mL three-neck round bottom flask was equipped with a vacuum outlet in the central port, and two rubber septum's in each side port with a thermometer in one to monitor the temperature of the solution. In the 50 mL three-neck round-bottom, cadmium oxide (4 mmol, 0.516 g), 22 mmol oleic acid (6.38 g) and 25 g octadecene were mixed, degassed by placing under a vacuum, while stirring, and heated to 100 °C with a heating mantle. The solution was then placed under N_2 atmosphere, pumped and purged three times, and heated to 260 °C with a heating mantle under N_2 until the solution was transparent indicating the formation of $Cd(oleate)_2$.[82] The black-colored selenium precursor solution, made by dispersing Se powder (2 mmol ,0.16 g) in 5 mL 1-octadecene, was then injected with a syringe into the solution through the rubber septum. The combination of colorless and black-colored solutions quickly turned a

bright orange–red color. After several minutes, the heating mantle was removed, the reaction was removed from N_2, and hexane was added to the solution to quench nanocrystal growth. The quantum dots were precipitated using hexane and ethanol through multiple rounds of centrifugation. The suspension was then decanted and dried under vacuum overnight. The powder X-ray diffraction pattern and ultraviolet-visible spectrum are consistent with the formation of zinc-blende CdSe quantum dots of the F43m space group and confirm a diameter of 2.5 nm (Figure 3.1). The synthesis was also confirmed by Fourier Transform Infrared Spectroscopy as shown in Figure 3.2. The FTIR spectrum for CdSe-oleate, Figure 3.2a, exhibits peaks at 2919 and 2844 cm^{-1} corresponding to C-H stretches, and peaks at 1537 and 1489 cm^{-1} are indicative of COO^- and can be attributed to the complexation of the group to Cd^{2+} centers.[129] The lack of broad OH stretches between 2500 and 3550 cm^{-1} confirm that the carboxylic acid groups of the oleic acid are bound to the surface of CdSe and the lack of a peak ~1700 indicating there is no free oleic acid present.[129]

3.2.9. Ligand-Exchange Protocols

Ligand exchanges were performed using literature procedures,[130,131] with the following modifications, shown in Figure 3.3. For synthesis of (2-mercaptoethanesulfonate)-capped CdSe quantum dots (CdSe-MES), purified CdSe quantum dots (20 mg) were suspended in 2 mL of chloroform and added to 15 mL of methanol solution containing 300 mg MES. The solution was refluxed overnight at 60 °C. The surface-modified QDs were then purified by sonication of the solution in an ultrasonic bath for approximately 5 min, until the mixture was sufficiently homogenous, followed by centrifugation at 12,000 rpm for 45 min in order to separate the quantum dots and to remove chloroform and excess MES. The FTIR spectrum for CdSe-MES,

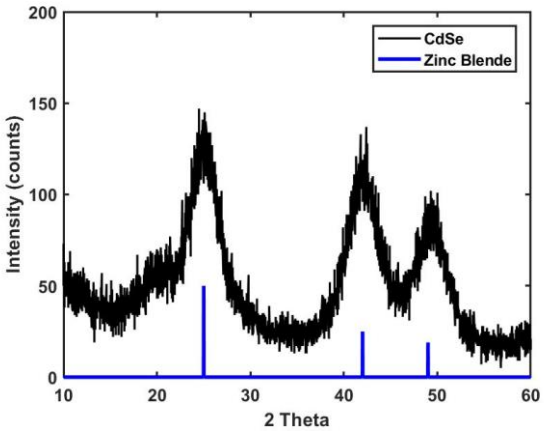

Figure 3.1 Powder X-ray diffraction patterns and thin-film X-ray diffraction patterns for CdSe quantum dots.

Figure 3.2b, exhibit strong peaks at 1178 and 1040 cm^{-1} corresponding to symmetric and asymmetric sulfonate stretches. The peak at 2924 cm^{-1} is indicative of a sulfur connected to a hydrocarbon chain and the broad peak at 3390 cm^{-1} is from methanol used in the synthesis and purification of the quantum dot. The presence of a peak at 1634 cm^{-1} indicates that there is free oleic acid still present and possibly still complexed to a small extent.

For synthesis of CdSe quantum dots with 4-mercaptophenol (CdSe-MPh), purified CdSe quantum dots (20 mg) were suspended in 2 mL of chloroform and added to 5 mL of deionized water. A drop of 10 mM NaOH was added to the solution and then the solution was stirred until the water layer turned orange in color and the chloroform layer became clear. The MPh-capped ligands were washed with methanol, centrifuged at 12,000 rpm for 45 min to separate the quantum dots from excess MPh, and allowed to dry. The FTIR spectrum for CdSe-MPh exhibits a peak at ~3000 cm^{-1} from the methanol used in the washing but is broader due to the aromatic hydroxyl group on MPh as well as the aromatic sulfur bound to the surface of CdSe which is

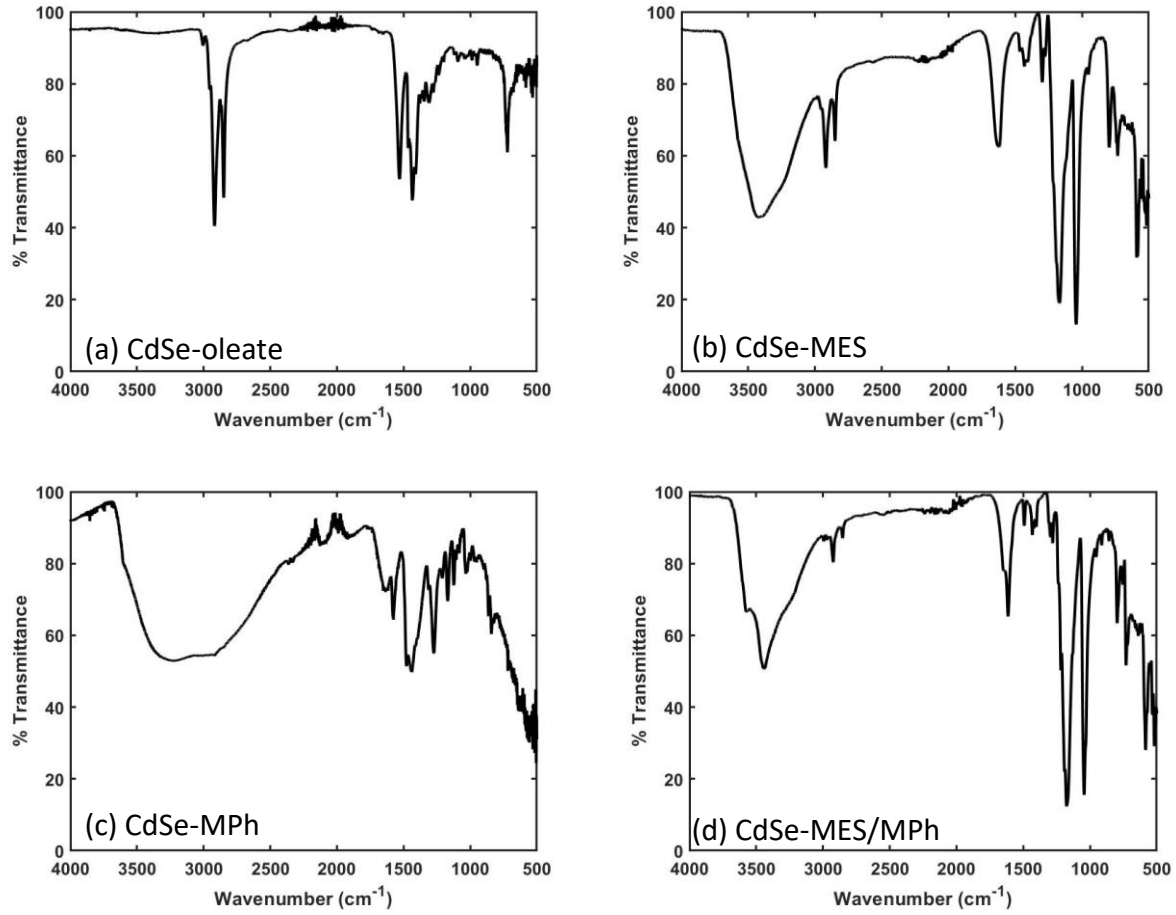

Figure 3.2 Fourier-Transform Infrared Spectroscopy for each CdSe quantum dot used in this study: (a) As synthesized CdSe with oleic acid capping ligands, CdSe-oleate, (b) CdSe with 2-mercaptoethanesulfonate capping ligands, CdSe-MES, (c) CdSe with 4-mercaptophenol capping ligands, CdSe-MPh, and (d) CdSe with mixed capping ligands, CdSe-MES/MPh.

typically found in the same region. Peaks corresponding to the aromatic ring are observed at ~ 3000 cm^{-1} for aromatic C–H stretches and peaks corresponding to C–C stretches are observed at 1570 cm^{-1} and as a doublet at 1456 cm^{-1}.

For synthesis of CdSe quantum dots with mixed ligands of 2-mercaptoethanesulfonate and 4-mercaptophenol (CdSe-MES/MPh) the ligand-exchange procedure for CdSe-MES was performed but an equivalent molar amount of 4-mercaptophenol was also added into the round-bottom flask. The FT-IR spectrum for CdSe-MES/MPh seems to exhibit more MES character than MPh

although the synthesis was performed using an equimolar amount of each. The broad O–H peak seen in CdSe-MPh decreased in size and shifted to 3446 cm^{-1} to more closely resemble CdSe-MES. The peaks at 1180 and 1029 cm^{-1} correspond to the MES ligand, however the peaks are distorted and slightly shifted in comparison to the FTIR of MES. The appearance of doublets at 1609 and 1186 cm^{-1} where the MES also shows peaks indicates that the distortion is caused by MPh. Further confirmation is presented in the next section from data obtained by electronic absorption spectroscopy.

3.3. Results and Discussion

CdSe quantum dots capped with oleate ligands were synthesized using modified literature procedures. Their electronic absorption spectrum when dissolved in chloroform exhibited a peak at 516 nm, which is consistent with a size of ~2.5 nm,[65,75,80,82,132] as well as two additional absorption peaks at 415 nm and 469 nm (Figure 3.4a). Using modified literature procedures, these ligands were replaced with either MES – as a control dye – or mixed MES-MPh ligands – as a proposed photoacid dye. The electronic absorption spectrum of CdSe-MES exhibited a peak at 519 nm, representing a small bathochromic shift from that of oleate-capped CdSe, a shoulder at 476 nm, representing a small bathochromic shift from that of oleate-capped CdSe, a peak at 421 nm, and a slight shoulder at 469 nm where a peak was observed in the oleate-capped CdSe spectrum.

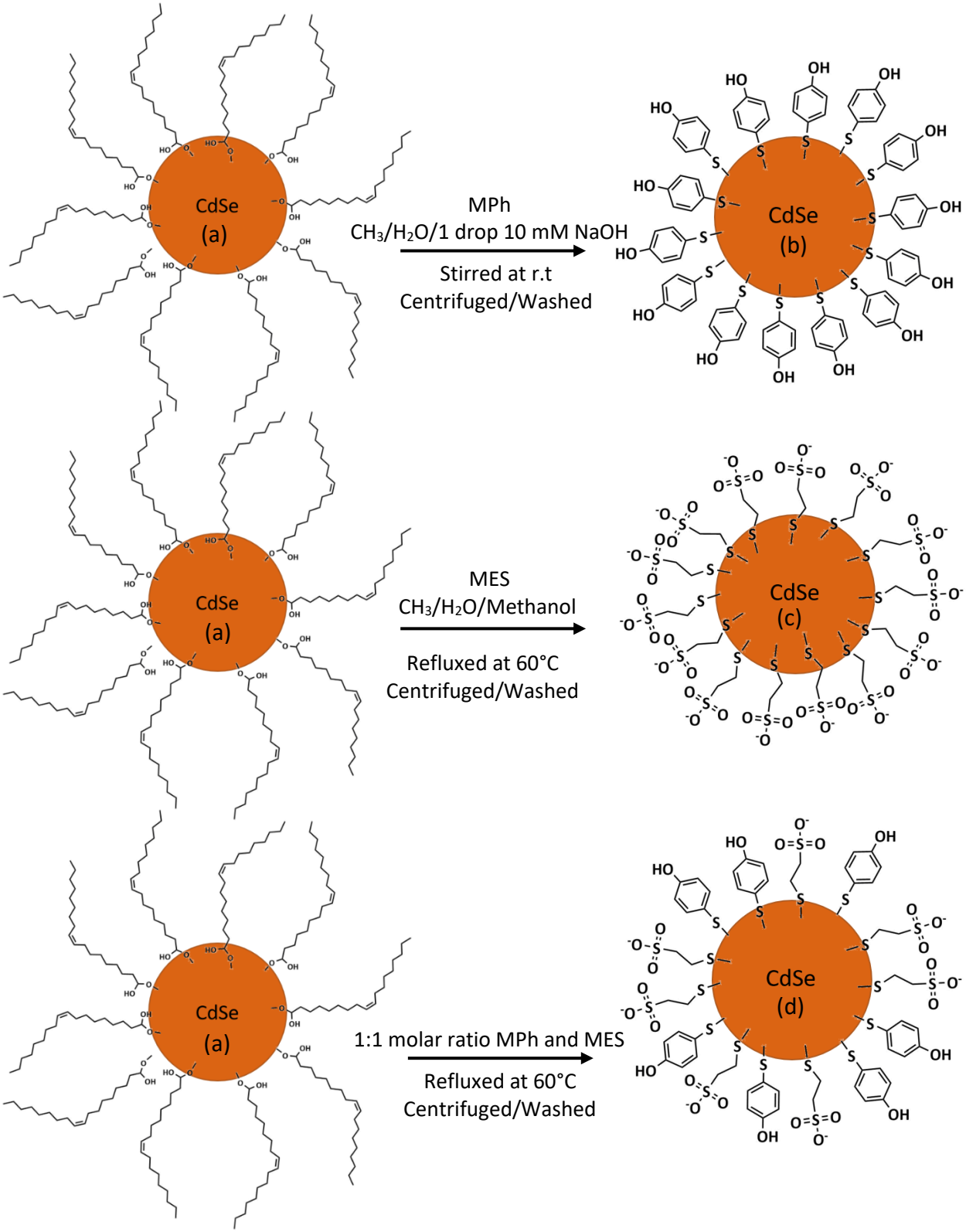

Figure 3.3 Scheme depicting ligand exchange protocol from initial oleate-capped quantum dots to photoacid quantum dots that are the focus of this work containing (b) CdSe-MPh, (c) CdSe-MES and (d) CdSe-MES/MPh mixed-ligand surfaces.

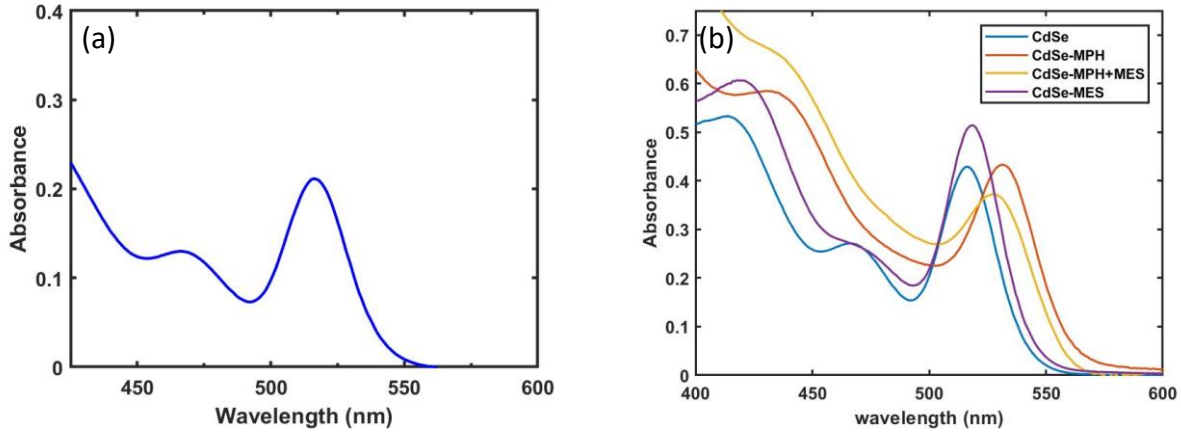

Figure 3.4 Electronic absorption spectra of (a) CdSe-oleate (b) ligand-exchanged CdSe.

The mixed-ligand quantum dot exhibited a peak at 527 nm, representing a larger bathochromic shift from the CdSe-oleate quantum dot, a shoulder at 432 nm, and no clear indication of the first excitonic peak in the 470 nm range. Photoluminescence could not be detected from any of the samples (Figure 3.4b).

Electrochemical impedance spectroscopy was used to measure the change in low-frequency impedance of the electrochemical cells in the dark and under illumination from a 405 nm light-emitting diode. Figure 3.5 shows the impedance response from solutions of CdSe quantum dots with different ligands. As a comparison, we measured the impedance response of the native CdSe-Oleate quantum dots where we did not expect to see a photoinduced change in the EIs spectrum. Moreover, due to their low solubility in water these data were measured using chloroform as the solvent, which resulted in much more noisy data due to the low conductivity of the solution. The trend in the shape of the data is consistent with a decrease in the charge-

transfer resistance by ~38%, plus other smaller effects. This effect is not observed in the ligand-exchanged samples. In the dark, all ligand-exchanged samples exhibit the same shaped-impedance spectrum which is analogous to that observed using control photoacid pyranine. Also analogous to control photoacid pyranine, illumination caused changes in the low-frequency region rather than the high-frequency region, which is consistent with a decrease in the diffusional mass transport resistance at the electrode as described in Chapter 2.

For the quantum dots that lack protic functional groups, CdSe-MES, there is only a small change in the photo-EIS spectra between condition in the dark and under illumination. For the quantum dots that contained protic functional groups, CdSe- MPh and CdSe-MES/MPh, the action of light clearly decreased diffusional resistance. In the case of CdSe-MPh, the change is much larger than when the ligands are mixed in CdSe-MES/MPh, but that is expected based on the photo-inactivity of CdSe-MES. Although the effects of light on the photo-EIS spectra are smaller for the mixed-ligand CdSe-MES/MPh, the addition of MES to the quantum dots allows for higher solubility and stability in solution. This provides clear evidence that we have, for the first time, demonstrated photoacidity from a quantum dot.

While the recently demonstrated electrochemical impedance spectroscopy technique utilized herein conclusively demonstrates that the quantum dots are photoacidic, we performed several control and additional measurements with a known photoacid, pyranine, to further support our claims. Because transport of protons is significantly faster than mass transport of photoacids, *any electrode* should be sensitive to the local change in ionic charge distribution upon photoexcitation, which would be manifest by a change in the open-circuit potential of the cell. Moreover, because excited-state photoacids are stronger electron-transfer reductants and

stronger electron-transfer oxidants than in their ground-states, a similar change in the open-circuit potential of the cell should result, but without a change in low-frequency impedance.

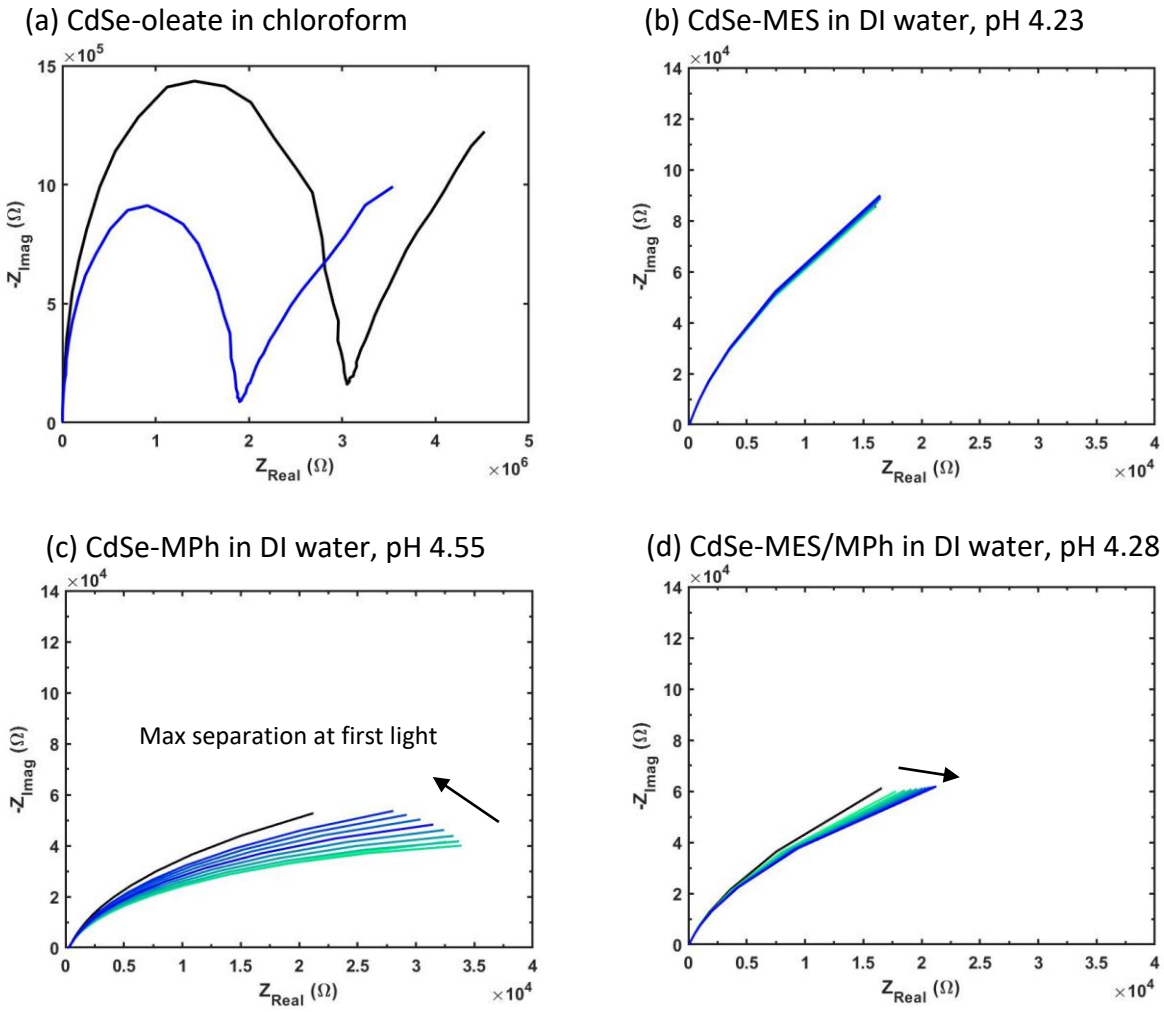

Figure 3.5 Time-dependent photo-EIS spectra plotted as a Nyquist plot for (a) CdSe-oleate quantum dots dissolved in chloroform, (b) CdSe-MES dissolved in deionized water (pH 4.23), (c) CdSe-MPh dissolved in deionized water (pH 4.55), and (d) CdSe-MES/MPh dissolved in deionized water (pH 4.28) showing dark equilibrated photo-EIS spectra (black) and photo-EIS spectra measured successively over time until a maximum separation is observed under illumination (green-to-blue).

(a) CdSe-MES in DI water, pH 4.23

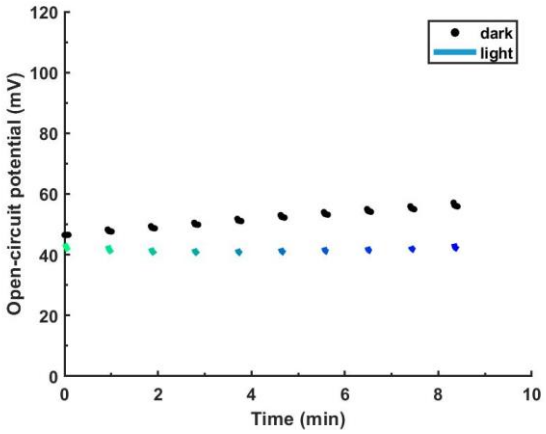

(b) CdSe-MPh in DI water, pH 4.55

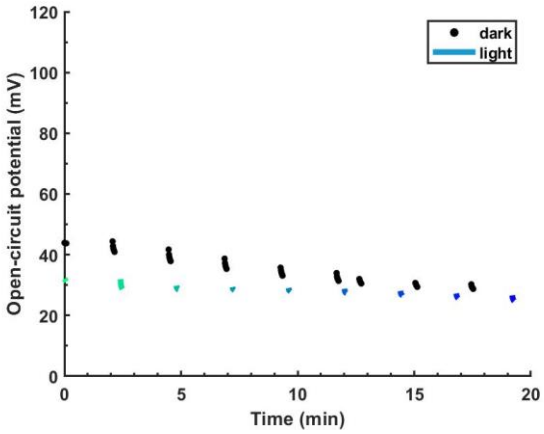

(c) CdSe-MES/MPh in DI water, pH 4.28

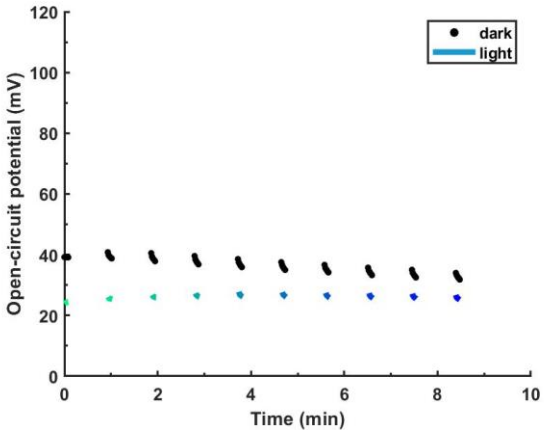

Figure 3.6 Open circuit potential data plotted over time taken in alternation with PEIS data (a) CdSe--MES dissolved in deionized water (pH 4.23), (b) CdSe-MPh dissolved in deionized water (pH 4.55), and (c) CdSe-MES/MPh dissolved in deionized water (pH 4.28) showing V_{OC} spectra in dark (black) and under continuous illumination. Light is shown as a green to blue for increasing time corresponding to identical color EIS data.

In addition, if both sides of the electrochemical cell are illuminated simultaneously with the same photon fluence, photoacidic behavior should result in a doubling of the decrease in the low-frequency impedance, while open-circuit potential changes due to either phenomenon should cancel out between the electrodes and result in little-to-no change. The open-circuit measurements are shown in Figure 3.6. In Figure 3.6c, for CdSe-MPh the maximum photo-EIS signal is seen immediately upon the first scan (1) and decreases thereafter (2).

In addition, Bode plots can be constructed using the photo-EIS data to allow us to analyze the phase and |Z| magnitude. The slope of the |Z| magnitude data and value for the phase confirm that the low-frequency data can be modeled with a parallel RC circuit element in place of the Warburg impedance element. Furthermore, because the experiments are performed using two-electrode measurements, this capacitance in the RC circuit can be removed. Thus, the Randles circuit used to analyze the photo-EIS data consisted of a constant phase element to model the diffuse–double-layer capacitance in parallel with a resistor to model the diffusional mass-transfer resistance and charge-transfer resistance. The Bode plots and circuit model are shown in Figure 3.7.

(a) CdSe-MES in DI water, pH 4.23

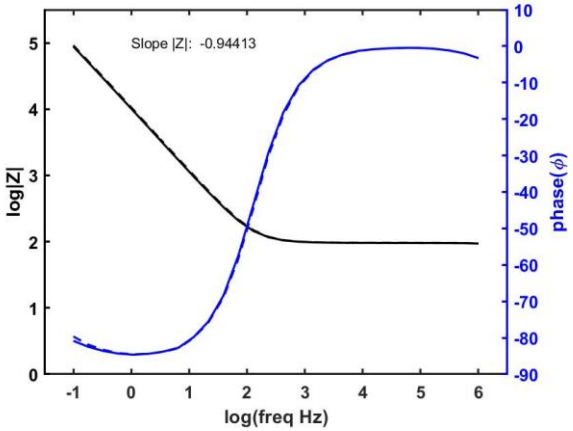

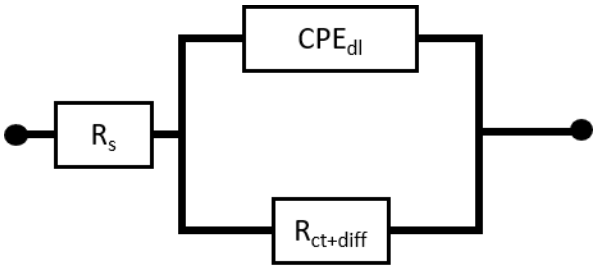

(b) CdSe-MPh in DI water, pH 4.55

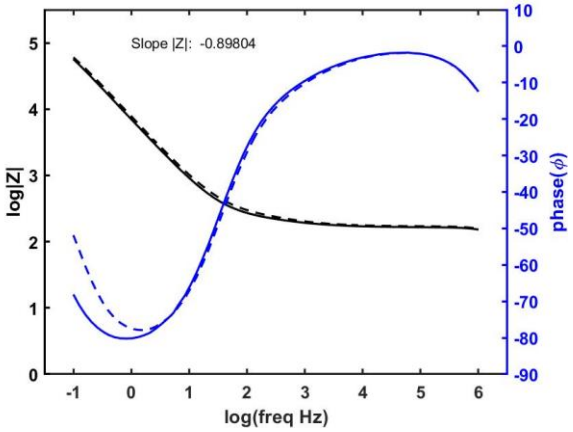

(c) CdSe-MES/MPh in DI water, pH 4.28

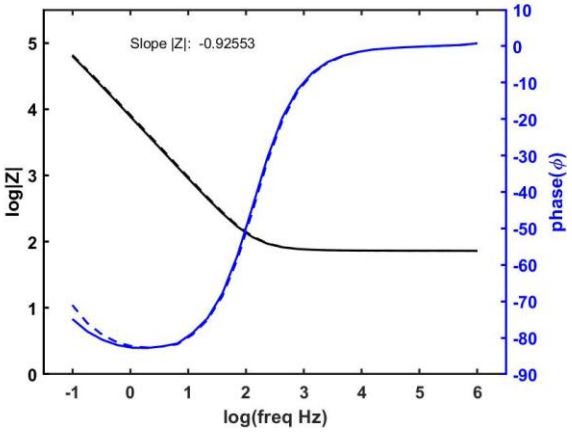

Figure 3.7 Time-dependent photo-EIS spectra plotted as Bode plots for (a) CdSe--MES dissolved in deionized water at pH 4.23, (b) CdSe-MPh dissolved in deionized water at pH 4.55, and (c) CdSe-MES/MPh dissolved in deionized water at pH 4.28. showing dark equilibrated photo-EIS spectra (solid) and photo-EIS spectra at the maximum separation under illumination (dotted).

The fits from the model are shown in Figure 3.8 with additional data provided in Table 3.1. The fits were done using EC-LAB Version 11.27 impedance fitting software from Bio-Logic Science Instruments (Method: Levenberg-Marquard, Weight: |Z|, and 5000 iterations). Both light and dark data were simulated using the circuit model shown in Figure 3.7 and data was tabulated as shown in Table 3.1. The values for solution resistance, R_s, are fixed based on the intersection of the data in the Nyquist plot with the x-axis. The values for the constant phase element, C_{dl}, and the ideality factor were averaged for both and used to remodel both light and dark spectra with constant values to study the deviation of resistance between dark and light measurements. The final values are shown in Table 3.2.

The values for solution resistance, R_s, are taken from the real axis of the Nyquist plot at the intersection of the x-axis. The values for the constant phase element, C_{dl}, and the ideality factor were averaged for data in the light and the dark because the values only differed by 4.7 – 9.0%. These average values were then used to remodel both light and dark spectra to study the deviation in mass-transport resistance and charge-transfer resistance between dark and light. The final values are shown in Table 2.2.

The trends in the data are as expected in that under illumination the sum of the charge-transfer resistance and the mass transport resistance decrease. This is similar to the results presented in Chapter 2 where a 55% decrease in resistance was seen for both 1 mM and 10 mM HPTS. The CdSe-MPh nanocrystal showed a 57.6% decrease in resistance whereas the mixed ligand, CdSe-MES/MPh, exhibited about half that at 23%. This is reasonable considering the ligand exchange synthesis was done using a 1:1 molar ratio of each and the CdSe-MES exhibits no significant change in resistance.

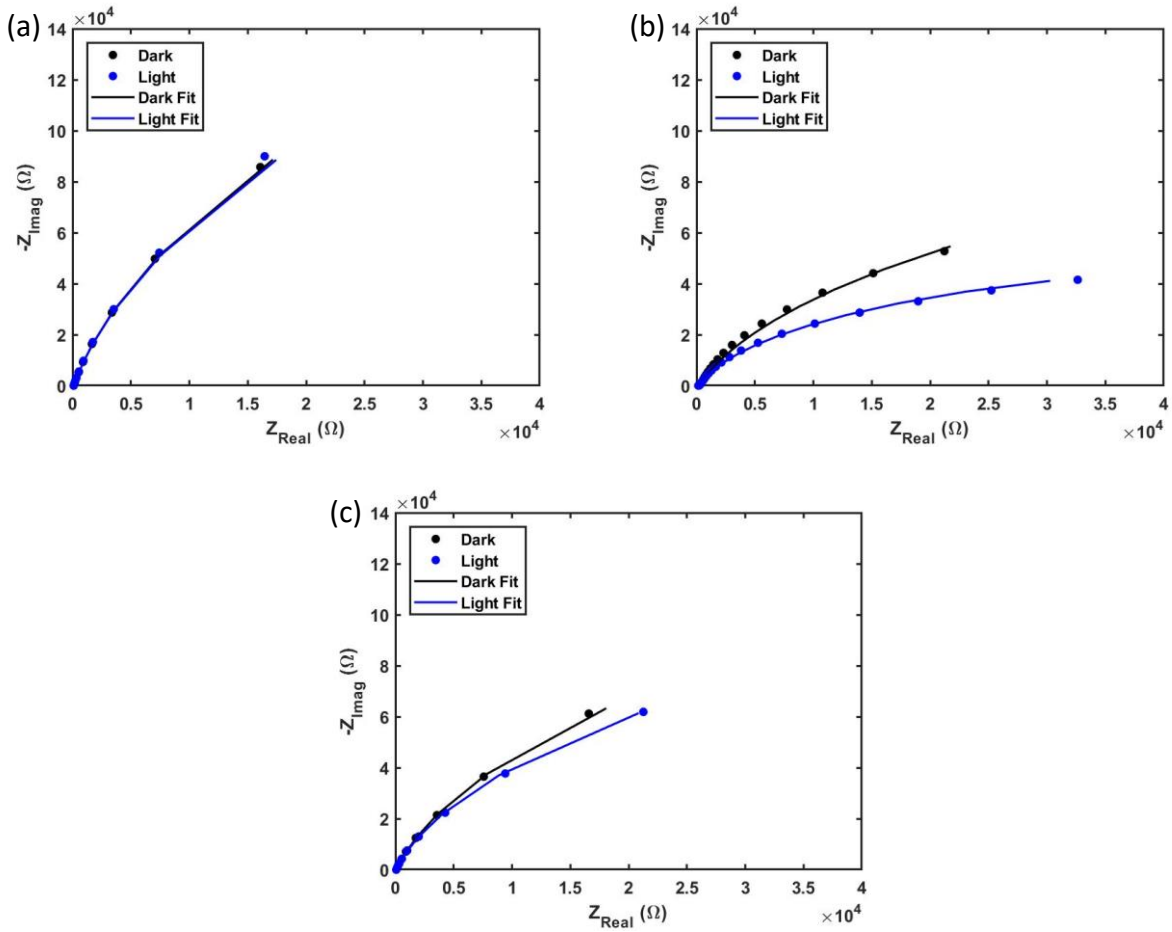

Figure 3.8 Fits of EIS data using EC-Lab Zfit by Biologic for (a) CdSe-MES, (b) CdSe-MPh, (c) CdSe-MES/MPh

Table 3.1 Data obtained for photo-EIS data using EC-Lab Zfit by Biologic for HPTS and MPTS. All components were varied except for the values for solution resistance, Rs, taken from the real axis of the Nyquist plot at the intersection of the x-axis.

Material	Circuit Element	Units	Dark	Deviation	Light	Deviation
CdSe-MPh	$\mathbf{R_s}$	Ω	168	x-int	168	x-int
	$\mathbf{CPE_{dl}}$	$F \bullet s^{(a-1)}$	25.4e-6	2.313e-9	23.37e-6	2.553e-6
	$\mathbf{a_{dl}}$		.9189	.5002	.8964	.5001
	$\mathbf{R_{ct+diff}}$	Ω	209379	65.95	106218	4.256
Material	**Circuit Element**	**Units**	**Dark**	**Deviation**	**Light**	**Deviation**
CdSe-MES	$\mathbf{R_s}$	Ω	95.4	x-int	96.2	x-int
	$\mathbf{CPE_{dl}}$	$F \bullet s^{(a-1)}$	17.35e-6	.910e-9	16.57e-6	.8212e-9
	$\mathbf{a_{dl}}$		.9501	.5003	.9497	.5001
	$\mathbf{R_{ct+diff}}$	Ω	817174	831.3	895673	911
Material	**Circuit Element**	**Units**	**Dark**	**Deviation**	**Light**	**Deviation**
CdSe-MES/MPh	$\mathbf{R_s}$	Ω	73.1	x-int	72.9	x-int
	$\mathbf{CPE_{dl}}$	$F \bullet s^{(a-1)}$	23.28e-6	2.178e-9	22.08e-6	2.178e-9
	$\mathbf{a_{dl}}$		.9337	.5003	.935	.5003
	$\mathbf{R_{ct+diff}}$	Ω	394449	333.2	288316	154.7

Table 3.2 The values for solution resistance, R_s, are taken from the real axis of the Nyquist plot at the intersection of the x-axis. The values for the constant phase element, C_{dl}, and the ideality factor were averaged for both and used to remodel both light and dark spectra with constant values to study the deviation of resistance between dark and light measurements.

Material	Circuit Element	Units	Dark	Deviation	Light	Deviation
CdSe-MPh	$\mathbf{R_s}$	Ω	168	x-int	168	x-int
	$\mathbf{CPE_{dl}}$	$F \bullet s^{(a-1)}$	24.39e-6		24.39e-6	
	$\mathbf{a_{dl}}$		.9077		.9077	
	$\mathbf{R_{ct+diff}}$	Ω	253844	.03078	107724	.2485
Material	**Circuit Element**	**Units**	**Dark**	**Deviation**	**Light**	**Deviation**
CdSe-MES	$\mathbf{R_s}$	Ω	95.4	x-int	96.2	x-int
	$\mathbf{CPE_{dl}}$	$F \bullet s^{(a-1)}$	16.96e-6		16.96e-6	
	$\mathbf{a_{dl}}$		.9499		.9499	
	$\mathbf{R_{ct+diff}}$	Ω	8.1e5	.01129	7.9e5	.0119
Material	**Circuit Element**	**Units**	**Dark**	**Deviation**	**Light**	**Deviation**
CdSe-MES/MPh	$\mathbf{R_s}$	Ω	73.1	x-int	72.9	x-int
	$\mathbf{CPE_{dl}}$	$F \bullet s^{(a-1)}$	22.68e-6		22.68e-6	
	$\mathbf{a_{dl}}$		.9344		.9344	
	$\mathbf{R_{ct+diff}}$	Ω	377939	.02221	291082	.02911

3.4. Conclusions

Confirmation of the first photo-acidic quantum dot was demonstrated using electrochemical impedance spectroscopy measurements in the dark and light. As seen with previous confirmations using known photoacids, the electrochemical impedance spectroscopy data presented a definitive change in the low-frequency impedance data between conditions in the dark and under illumination. In addition, the CdSe-MES nanocrystal was used as a control, as MES is used as a water-solubilizing ligand and exhibited no change between dark and light conditions. Ligand exchange of CdSe-oleate quantum dots with water-solubilizing 2-mercaptoethanesulfonate and the photoacidic ligand, 4-mercaptophenol, was completed and characterized using electronic absorption spectroscopy, Fourier-Transform infrared spectroscopy, and X-ray diffraction. The trends were consistent with decrease in the mass-transport resistance of protons under illumination due to their photo-generation via optical excitation that followed the Beer–Lambert law. Open-circuit potential measurements in the light and dark further confirmed this hypothesis.

REFERENCES

(1) Clark, C. E. Renewable Energy R & D Funding History : A Comparison with Funding for Nuclear Energy , Fossil Energy , Energy Efficiency , and Electric Systems R & D. **2018**.

(2) Gielen, D.; Boshell, F.; Saygin, D.; Bazilian, M. D.; Wagner, N.; Gorini, R. The Role of Renewable Energy in the Global Energy Transformation. *Energy Strateg. Rev.* **2019**, *24* (January), 38–50.

(3) Kaygusuz, K. Energy for Sustainable Development : A Case of Developing Countries. *Renew. Sustain. Energy Rev.* **2012**, *16* (2), 1116–1126.

(4) Crabtree, George, W., Lewis, Nathan, S. Solar Energy Conversion. *Phys. Today* **2007**, No. 3, 37.

(5) National Renewable Energy Laboratory. *Research Cell Efficiency Records*; 2017.

(6) SunPower Corporation. *Engineered for Peace of Mind X-Series Residential Solar X21-255*.

(7) Fu, R.; Feldman, D.; Margolis, R.; Woodhouse, M.; Ardani, K. *U.S. Solar Photovoltaic System Cost Benchmark: Q1 2017*; 2017.

(8) IRENA(2018). *Power Generation Costs in 2017,*; 2018; Vol. Abu Dhabi.

(9) International Energy Agency. *World Energy Balances: Overview*; 2018.

(10) International Energy Agency. *Electricity Information 2018 Overview*; 2019.

(11) International Energy Agency. *Global Energy & CO2 Status Report: The Latest Trends in Energy and Emissions in 2018*; 2019.

(12) Sørensen, B. Energy and Resources. *Science (80-.).* **1975**, *189* (4199), 255 LP – 260.

(13) Hohmeyer, O. H.; Bohm, S. Trends toward 100% Renewable Electricity Supply in Germany and Europe: A Paradigm Shift in Energy Policies. *Wiley Interdiscip. Rev. Energy Environ.* **2015**, *4* (1), 74–97.

(14) Zappa, W.; Junginger, M.; van den Broek, M. Is a 100% Renewable European Power System Feasible by 2050? *Appl. Energy* **2019**, *233–234*, 1027–1050.

(15) Connolly, D.; Lund, H.; Mathiesen, B. V.; Leahy, M. The First Step towards a 100% Renewable Energy-System for Ireland. *Appl. Energy* **2011**, *88* (2), 502–507.

(16) Krakowski, V.; Assoumou, E.; Mazauric, V.; Maïzi, N. Feasible Path toward 40–100% Renewable Energy Shares for Power Supply in France by 2050: A Prospective Analysis. *Appl. Energy* **2016**, *171*, 501–522.

(17) Krajačić, G.; Duić, N.; Carvalho, M. da G. How to Achieve a 100% RES Electricity Supply for Portugal? *Appl. Energy* **2011**, *88* (2), 508–517.

(18) Weiss, O.; Bogdanov, D.; Salovaara, K.; Honkapuro, S. Market Designs for a 100% Renewable Energy System: Case Isolated Power System of Israel. *Energy* **2017**, *119*, 266–277.

(19) Esteban, M.; Portugal-Pereira, J.; Mclellan, B. C.; Bricker, J.; Farzaneh, H.; Djalilova, N.; Ishihara, K. N.; Takagi, H.; Roeber, V. 100% Renewable Energy System in Japan: Smoothening and Ancillary Services. *Appl. Energy* **2018**, *224*, 698–707.

(20) Mason, I. G.; Page, S. C.; Williamson, A. G. A 100% Renewable Electricity Generation System for New Zealand Utilising Hydro, Wind, Geothermal and Biomass Resources. *Energy Policy* **2010**, *38* (8), 3973–3984.

(21) Jacobson, M. Z.; Delucchi, M. A.; Bazouin, G.; Bauer, Z. A. F.; Heavey, C. C.; Fisher, E.; Morris, S. B.; Piekutowski, D. J. Y.; Vencill, T. A.; Yeskoo, T. W. 100% Clean and Renewable Wind, Water, and Sunlight (WWS) All-Sector Energy Roadmaps for the 50 United States. *Energy Environ. Sci.* **2015**, *8* (7), 2093–2117.

(22) Hand, M. M. .; Baldwin, S.; DeMeo, E.; Reilly, J.M.; Mai, T.; Arent, D.; Porro, G.; Meshek, M.; Sandor, D. *Renewable Electricity Futures Study. Volume 1: Exploration of High-Penetration Renewable Electricity Futures*; 2012; Vol. 1.

(23) Hand, M. M. .; Baldwin, S.; DeMeo, E.; Reilly, J.M.; Mai, T.; Arent, D.; Porro, G.; Meshek, M.; Sandor, D. *Renewable Electricity Futures Study: Renewable Electricity Generation and Storage Technologies: Volume 2 of 4*; 2012; Vol. 2.

(24) Williams, R. Becquerel Photovoltaic Effect in Binary Compounds. *J. Chem. Phys.* **1960**, *32* (5), 1505–1514.

(25) Cook, G.; Billman, L.; Adcock, R. *Photovoltaic Fundamentals*; 1990.

(26) Einstein, A. On a Heuristic Point of View about the Creation and Conversion of Light (German: Über Einen Die Erzeugung Und Verwandlung Des Lichtes Betreffenden Heuristischen Gesichtspunkt). *Ann. Phys.* **1905**, *322* (6), 132–148.

(27) Hoang, S. The Environmental History of Solar Photovoltaic Cells. *Student Libr. Res. Award.* **2017**.

(28) Abdelhady, S.; Abd-Elhady, M. S.; Fouad, M. M. An Understanding of the Operation of Silicon Photovoltaic Panels. *Energy Procedia* **2017**, *113*, 466–475.

(29) Nocera, D. G. Solar Fuels and Solar Chemicals Industry. *Acc. Chem. Res.* **2017**, *50* (3), 616–619.

(30) Graetzel, M. Artificial Photosynthesis: Water Cleavage into Hydrogen and Oxygen by Visible Light. *Acc. Chem. Res.* **1981**, *14* (12), 376–384.

(31) Brotosudarmo, T. H. P.; Prihastyanti, M. N. U.; Gardiner, A. T.; Carey, A.-M.; Cogdell, R. J. The Light Reactions of Photosynthesis as a Paradigm for Solar Fuel Production. *Energy Procedia* **2014**, *47*, 283–289.

(32) Cogdell, R. J.; Brotosudarmo, T. H.; Gardiner, A. T.; Sanchez, P. M.; Cronin, L. Artificial Photosynthesis – Solar Fuels: Current Status and Future Prospects. *Biofuels* **2010**, *1* (6), 861–876.

(33) Calvin, M. PHOTOSYNTHESIS AS A RESOURCE FOR ENERGY AND MATERIALS. *Photochem. Photobiol.* **1976**, *23* (6), 425–444.

(34) Calvin, M. Artificial Photosynthesis. *J. Memb. Sci.* **1987**, *33* (2), 137–149.

(35) Ciamician, G. The Photochemistry of the Future Author (s): Giacomo Ciamician Published by : American Association for the Advancement of Science Stable URL : Http://Www.Jstor.Org/Stable/1637055 Accessed : 03-03-2016 13 : 55 UTC Your Use of the JSTOR Archive Indicates. *Science (80-.).* **1912**, *36* (926), 385–394.

(36) El-Khouly, M. E.; El-Mohsnawy, E.; Fukuzumi, S. Solar Energy Conversion: From Natural to Artificial Photosynthesis. *J. Photochem. Photobiol. C Photochem. Rev.* **2017**, *31*, 36–83.

(37) Deisenhofer, J.; Michel, H. The Photosynthetic. **1989**, *8* (8), 2149–2170.

(38) Barber, J. Photosynthetic Energy Conversion: Natural and Artificial. *Chem. Soc. Rev.* **2009**, *38* (1), 185–196.

(39) Maeda, K. Z - Scheme Water Splitting Using Two Di Ff Erent Semiconductor Photocatalysts. *ACS Catal.* **2013**, *2*.

(40) Fujita, E.; Muckerman, J. T. Catalytic Reactions Using Transition-Metal-Complexes Toward Solar Fuel Generation. *Bull. Japan Soc. Coord. Chem.* **2008**, *51* (0), 41–54.

(41) Hambourger, Michael, Moore, Gary F., Kramer, David M., Gust, Devens, Moore, Ana L., Moore, T. A. Biology and Technology for Photochemical Fuel Production. *Chem. Soc. Rev.* **2008**, *38* (1), 25–35.

(42) Armaroli, N.; Balzani, V. Solar Electricity and Solar Fuels: Status and Perspectives in the Context of the Energy Transition. *Chem. - A Eur. J.* **2016**, *22* (1), 32–57.

(43) Walker, D. A. Biofuels, Facts, Fantasy, and Feasibility. *J. Appl. Phycol.* **2009**, *21* (5), 509–517.

(44) Zhu, X.-G.; Long, S. P.; Ort, D. R. Improving Photosynthetic Efficiency for Greater Yield. *Annu. Rev. Plant Biol.* **2010**, *61* (1), 235–261.

(45) Blankenship, R. E.; Blankenship, D. M.; Tiede, J.; Barber, G. W.; Brudvig, G.; Fleming, M.; Ghirardi, M. R.; Gunner, W.; Junge, D. M.; Kramer, A.; et al. Comparing Photosynthetic and Photovoltaic Efficiencies and Recognizing the Potential for Improvement. *Science (80-.).* **2011**, *332* (6031), 805–809.

(46) Bonke, S. A.; Wiechen, M.; MacFarlane, D. R.; Spiccia, L. Renewable Fuels from Concentrated Solar Power: Towards Practical Artificial Photosynthesis. *Energy Environ. Sci.* **2015**, *8* (9), 2791–2796.

(47) Singh, M. R.; Goodpaster, J. D.; Weber, A. Z.; Head-Gordon, M.; Bell, A. T. Mechanistic Insights into Electrochemical Reduction of CO 2 over Ag Using Density Functional Theory and Transport Models . *Proc. Natl. Acad. Sci.* **2017**, *114* (42), E8812–E8821.

(48) Windle, C. D.; Perutz, R. N. Advances in Molecular Photocatalytic and Electrocatalytic CO 2 Reduction. *Coord. Chem. Rev.* **2012**, *256* (21–22), 2562–2570.

(49) Herron, J. A.; Kim, J.; Upadhye, A. A.; Huber, G. W.; Maravelias, C. T. A General Framework for the Assessment of Solar Fuel Technologies. *Energy Environ. Sci.* **2015**, *8* (1), 126–157.

(50) Harriman, A. The Photodissociation of Water. *Platin. Met. Rev* **1983**, *27* (3), 102–107.

(51) Balzani, V.; Bergamini, G.; Ceroni, P. Light: A Very Peculiar Reactant and Product. *Angew. Chemie Int. Ed.* **2015**, *54* (39), 11320–11337.

(52) Lozier, R. H.; Bogomolni, R. A.; Stoeckenius, W. Bacteriorhodopsin: A Light-Driven Proton Pump in Halobacterium Halobium. *Biophys. J.* **1975**, *15* (9), 955–962.

(53) Hayashi, S.; Tajkhorshid, E.; Schulten, K. Molecular Dynamics Simulation of Bacteriorhodopsin's Photoisomerization Using Ab Initio Forces for the Excited Chromophore. *Biophys. J.* **2003**, *85* (3), 1440–1449.

(54) Lanyi, J. K. Proton Transfers in the Bacteriorhodopsin Photocycle. *Biochim. Biophys. Acta - Bioenerg.* **2006**, *1757* (8), 1012–1018.

(55) Simkovitch, R.; Shomer, S.; Gepshtein, R.; Huppert, D. How Fast Can a Proton-Transfer Reaction Be beyond the Solvent-Control Limit? *J. Phys. Chem. B* **2015**, *119* (6), 2253–2262.

(56) Amdursky, N.; Simkovitch, R.; Huppert, D. Excited-State Proton Transfer of Photoacids Adsorbed on Biomaterials. **2014**.

(57) Simkovitch, R.; Akulov, K.; Shomer, S.; Roth, M. E.; Shabat, D.; Schwartz, T.; Huppert, D. Comprehensive Study of Ultrafast Excited-State Proton Transfer in Water and D2O Providing the Missing RO-···H+ Ion-Pair Fingerprint. *J. Phys. Chem. A* **2014**, *118* (25), 4425–4443.

(58) Mondal, S. K.; Sahu, K.; Ghosh, S.; Sen, P.; Bhattacharyya, K. Excited-State Proton Transfer from Pyranine to Acetate in γ-Cyclodextrin and Hydroxypropyl γ-Cyclodextrin. *J. Phys. Chem. A* **2006**, *110* (51), 13646–13652.

(59) Finkler, B.; Spies, C.; Vester, M.; Walte, F.; Omlor, K.; Riemann, I.; Zimmer, M.; Stracke, F.; Gerhards, M.; Jung, G. Highly Photostable "Super"-Photoacids for Ultrasensitive Fluorescence Spectroscopy. *Photochem. Photobiol. Sci.* **2014**, *13* (3), 548–562.

(60) Johns, V. K.; Wang, Z.; Li, X.; Liao, Y. Physicochemical Study of a Metastable-State Photoacid. *J. Phys. Chem. A* **2013**, *117* (49), 13101–13104.

(61) Donnell, R. M. O.; Sampaio, R. N.; Li, G.; Johansson, P. G.; Ward, C. L.; Meyer, G. J. Photoacidic and Photobasic Behavior of Transition Metal Compounds with Carboxylic Acid Group(S). *J. Am. Chem. Soc.* **2016**, *138*, 3891–3903.

(62) Grabowski, Z. R., Rubaszewska, W. Generalised Forster Cycle. *J* **1976**.

(63) Berland, B. Photovoltaic Technologies Beyond the Horizon: Optical Rectenna Solar Cell, Final Report, 1 August 2001-30 September 2002. **2003**, No. February.

(64) Čapek, R. K.; Moreels, I.; Lambert, K. Optical Properties of Zincblende Cadmium Selenide Quantum Dots Supporting Information. *J.* **2010**, 1–4.

(65) Zlateva, G.; Zhelev, Z.; Bakalova, R.; Kanno, I. Precise Size Control and Synchronized Synthesis of Six Colors of CdSe Quantum Dots in a Slow-Increasing Temperature Gradient. *Inorg. Chem.* **2007**, *46* (16), 6212–6214.

(66) De Mello Donegá, C.; Hickey, S. G.; Wuister, S. F.; Vanmaekelbergh, D.; Meijerink, A. Single-Step Synthesis to Control the Photoluminescence Quantum Yield and Size Dispersion of CdSe Nanocrystals. *J. Phys. Chem. B* **2003**, *107* (2), 489–496.

(67) Simkovitch, R.; Shomer, S.; Gepshtein, R.; Roth, M. E.; Shabat, D.; Huppert, D. Comparison of the Rate of Excited-State Proton Transfer from Photoacids to Alcohols and Water. *J. Photochem. Photobiol. A Chem.* **2014**, *277*, 90–101.

(68) Tolbert, L. M.; Solntsev, K. M. Excited-State Proton Transfer: From Constrained Systems to "Super " Photoacids to Superfast Proton Transfer. *Acc. Chem. Res.* **2002**, *35* (1), 19–27.

(69) Agmon, N. Elementary Steps in Excited-State Proton Transfer. *J. Phys. Chem. A* **2005**, *109* (1), 13–35.

(70) Mohammed, O. F.; Dreyer, J.; Magnes, B. Z.; Pines, E.; Nibbering, E. T. J. Solvent-Dependent Photoacidity State of Pyranine Monitored by Transient Mid-Infrared Spectroscopy. *ChemPhysChem* **2005**, *6* (4), 625–636.

(71) Liu, I.-S.; Lo, H.-H.; Chien, C.-T.; Lin, Y.-Y.; Chen, C.-W.; Chen, Y.-F.; Su, W.-F.; Liou, S.-C. Enhancing Photoluminescence Quenching and Photoelectric Properties of CdSe Quantum Dots with Hole Accepting Ligands. *J. Mater. Chem.* **2008**, *18* (6), 675.

(72) Wuister, S. F.; De Mello Donegá, C.; Meijerink, A. Influence of Thiol Capping on the Exciton Luminescence and Decay Kinetics of CdTe and CdSe Quantum Dots. *J. Phys. Chem. B* **2004**, *108* (45), 17393–17397.

(73) Jeong, S.; Achermann, M.; Nanda, J.; Ivanov, S.; Klimov, V. I.; Hollingsworth, J. A. Effect of the Thiol-Thiolate Equilibrium on the Photophysical Properties of Aqueous CdSe/ZnS Nanocrystal Quantum Dots. *J. Am. Chem. Soc.* **2005**, *127* (29), 10126–10127.

(74) Liang, Y.; Thorne, J. E.; Parkinson, B. A. Controlling the Electronic Coupling between CdSe Quantum Dots and Thiol Capping Ligands via PH and Ligand Selection. *Langmuir* **2012**, *28* (30), 11072–11077.

(75) Baker, D. R.; Kamat, P. V. Tuning the Emission of CdSe Quantum Dots by Controlled Trap Enhancement. *Langmuir* **2010**, *26* (13), 11272–11276.

(76) Aldana, J.; Wang, Y. A.; Peng, X. Photochemical Instability of CdSe Nanocrystals Coated by Hydrophilic Thiols. *J. Am. Chem. Soc.* **2001**, *123* (36), 8844–8850.

(77) Avellini, T.; Amelia, M.; Credi, A.; Silvi, S.; Ciamician, C. G. Effect of Protons on CdSe and CdSe − ZnS Nanocrystals in Organic Solution. *Langmuir* **2013**, *29*, 13352–13358.

(78) Carvalho, M. S.; Raphael, E.; Dantas, C.; Ferrari, J. L.; Bosco, C. D.; Caxias, C.; Caxias, D. Synthesis , Optical Characterization , and Size Distribution Determination by Curve Resolution Methods of Water-Soluble CdSe Quantum Dots. **2016**, *19* (6), 1407–1416.

(79) Yu, W. W.; Qu, L.; Guo, W.; Peng, X. Experimental Determination of the Extinction Coefficient of CdTe , CdSe , and CdS Nanocrystals Experimental Determination of the Extinction Coefficient of CdTe , CdSe , and CdS Nanocrystals. *Chem. Mater.* **2003**, *15* (14), 2854–2860.

(80) Zhang, J.; Gao, J.; Church, C. P.; Miller, E. M.; Luther, J. M.; Klimov, V. I.; Beard, M. C. PbSe Quantum Dot Solar Cells with More than 6% Efficiency Fabricated in Ambient Atmosphere. *Nano Lett.* **2014**, *14*, 6010–6015.

(81) Knauf, R. R.; Lennox, J. C.; Dempsey, J. L. Quantifying Ligand Exchange Reactions at CdSe Nanocrystal Surfaces. *Chem. Mater.* **2016**, *28* (13), 4762–4770.

(82) Knauf, R. R.; Lennox, J. C.; Dempsey, J. L. Quantifying Ligand Exchange Reactions at CdSe Nanocrystal Surfaces. *Chem. Mater.* **2016**, *28* (13), 4762–4770.

(83) Haghighat, S.; Ostresh, S.; Dawlaty, J. M. Controlling Proton Conductivity with Light: A Scheme Based on Photoacid Doping of Materials. *J. Phys. Chem. B* **2016**, *120* (5), 1002–1007.

(84) Lasia, A. *Electrochemical Impedance Spectroscopy and Its Applications.Pdf*; Springer: London, 1999.

(85) Orazem, Mark E., Tribollet, B. *Electrochemical Impedance Spectroscopy*; John Wiley & Sons: Hoboken, NJ, 2008.

(86) Barsoukov, E.; Macdonald, J. R. *Impedance Spectroscopy - Theory, Experiment, and Applications*; John Wiley & Sons: Hoboken, NJ, 2005; Vol. 177.

(87) Bard, Allen J., L. R. F. *Electrochemical Methods: Fundamentals and Applications*, 2nd ed.; John Wiley & Sons, 2001.

(88) Bisquert, Juan, Compte, A. Theory of the Electrochemical Impedance of Anomalous Diffusion. *J. Electroanal. Chem.* **2001**, *499*, 112–120.

(89) Bisquert, J. Theory of the Impedance of Electron Diffusion and Recombination in a Thin Layer. *J. Phys. Chem. B* **2002**, *106* (2), 325–333.

(90) Bisquert, J.; Garcia-Belmonte, G.; Fabregat-Santiago, F.; Bueno, P. R. Theoretical Models for Ac Impedance of Finite Diffusion Layers Exhibiting Low Frequency Dispersion. *J. Electroanal. Chem.* **1999**, *475* (2), 152–163.

(91) Chandrasekhar, S. Bisquert Equations Paper.Pdf. *Rev. Mod. Phys.* **1943**, *15* (1), 1–89.

(92) Spry, D. B.; Goun, A.; Fayer, M. D. Deprotonation Dynamics and Stokes Shift of Pyranine (HPTS). **2007**, 230–237.

(93) Simkovitch, R.; Shomer, S.; Gepshtein, R.; Roth, M. E.; Shabat, D.; Huppert, D. Comparison of the Rate of Excited-State Proton Transfer from Photoacids to Alcohols and Water. *J. Photochem. Photobiol. A Chem.* **2014**, *277*, 90–101.

(94) Vos, G. Excited-State Acid-Base Properties of Inorganic Compounds. *Polyhedron* **1992**, *11* (18), 2285–2299.

(95) Giordano, P. J., Bock, C. R., Wrighton, M. S., Interrante, L. V., Williams, R. F. X. Excited State Proton Transfer of a Metal Complex: Determination of the Acid Dissociation Constant for a Metal-to-Ligand Charge Transfer State of a Ruthenium(II) Complex. *J. Am. Chem. Soc.* **1977**, *99* (9), 3187–3189.

(96) Hicks, C.; Ye, G.; Levi, C.; Gonzales, M.; Rutenburg, I.; Fan, J.; Helmy, R.; Kassis, A.; Gafney, H. D. Excited-State Acid – Base Chemistry of Coordination Complexes. *Coord. Chem. Rev.* **2001**, *211*, 207–222.

(97) Forster, T. No Title. *Elektrochem* **1950**, *54* (42), 531.

(98) Shi, Z.; Peng, P.; Strohecker, D.; Liao, Y. Long-Lived Photoacid Based upon a Photochromic Reaction. *J. Am. Chem. Soc.* **2011**, *133* (37), 14699–14703.

(99) Abeyrathna, N.; Liao, Y. A Reversible Photoacid Functioning in PBS Buffer under Visible Light. *J. Am. Chem. Soc.* **2015**, *137*, 11282–11284.

(100) Sheng, Y.; Leszczynski, J.; Garcia, A. A.; Rosario, R. Comprehensive Theoretical Study of the Conversion Reactions of Spiropyrans : Substituent and Solvent Effects. *J. Phys. Chem. B* **2004**, *108*, 16233–16243.

(101) Buback, J.; Nuernberger, P.; Kullmann, M.; Langhojer, F.; Schmidt, R.; Frank, W.; Brixner, T. Ring-Closure and Isomerization Capabilities of Spiropyran-Derived Merocyanine Isomers. *J. Phys. Chem. A* **2011**, *115*, 3924–3935.

(102) Nakazumi, H.; Maeda, K.; Yagi, S.; Kitao, T. Novel Merocyanine Dyes Are Converted into the Spiropyran Form by Irradiation with Visible Light. *J. Chem. Soc. Chem. Commun.* **1992**, No. 17, 1188–1189.

(103) Eilmes, A. Spiropyran to Merocyanine Conversion: Explicit versus Implicit Solvent Modeling. *J. Phys. Chem. A* **2013**, *117* (12), 2629–2635.

(104) Lakowicz, J. R. *Principles of Fluorescence Spectroscopy*, 3rd ed.; Springer: New York, 2006.

(105) Spies, C.; Finkler, B.; Acar, N.; Jung, G. Solvatochromism of Pyranine-Derived Photoacids †. *Phys. Chem. Chem. Phys.* **2013**, *15*, 19893–19905.

(106) White, W.; Sanborn, C. D.; Reiter, R. S.; Fabian, D. M.; Ardo, S. Observation of Photovoltaic Action from Photoacid-Modified Nafion Due to Light-Driven Ion Transport. *J. Am. Chem. Soc.* **2017**, *139* (34), 11726–11733.

(107) Spry, D. B.; Goun, A.; Bell, C. B.; Fayer, M. D. Identification and Properties of the 1L a and 1L b States of Pyranine. *J. Chem. Phys.* **2006**, *125* (14), 1–12.

(108) Awasthi, A. A.; Singh, P. K. Excited-State Proton Transfer on the Surface of a Therapeutic Protein, Protamine. *J. Phys. Chem. B* **2017**, *121* (45), 10306–10317.

(109) Oscar, B. G.; Liu, W.; Rozanov, N. D.; Fang, C. Ultrafast Intermolecular Proton Transfer to a Proton Scavenger in an Organic Solvent. *Phys. Chem. Chem. Phys.* **2016**, *18* (37), 26151–26160.

(110) Tran-Thi, T. H.; Gustavsson, T.; Prayer, C.; Pommeret, S.; Hynes, J. T. Primary Ultrafast Events Preceding the Photoinduced Proton Transfer from Pyranine to Water. *Chem. Phys. Lett.* **2000**, *329* (5–6), 421–430.

(111) Förster, T.; Völker, S. Kinetics of Proton Transfer Reactions Involving Hydroxypyrene-Trisulphonate in Aqueous Solution by Nanosecond Laser Absorption Spectroscopy. *Chem. Phys. Lett.* **1975**, *34* (1), 1–6.

(112) Vadim F. LvovichWiley, A. J. *Applications to Electrochemical and Dielectric Phenomena*; 2012.

(113) Weber, K. The Close Relationship of Flourescence Obliteration of Photochemical Reactions. *Z. Phys. Chem., Abt. B* **1931**, *15*, 18–44.

(114) Arnaut, L. G.; Formosinho, S. J. Excited-State Proton Transfer Reactions I. Fundamentals and Intermolecular Reactions. *J. Photochem. Photobiol. A Chem.* **1993**, *75*, 1–20.

(115) Onufriev, A.; Case, D. A.; Ullmann, G. M. A Novel View of PH Titration in Biomolecules. *Biochemistry* **2001**, *40* (12), 3413–3419.

(116) Hallett-Tapley, G. L.; Wee, T. L.; Tran, H.; Rananavare, S. B.; Blackwell, J. M.; Scaiano, J. C. Single Component Photoacid/Photobase Generators: Potential Applications in Double Patterning Photolithography. *J. Mater. Chem. C* **2013**, *1* (15), 2657–2665.

(117) Martin, C. J.; Rapenne, G.; Nakashima, T.; Kawai, T. Recent Progress in Development of Photoacid Generators. *J. Photochem. Photobiol. C Photochem. Rev.* **2018**, *34*, 41–51.

(118) Crivello, J.V., Conlon, D.A., Lee, J. . The Synthesis and Characterization of Cationic Photoinitiators Bearing Two and Three Photoactive Triarylsulfonium Groups in the Same Molecule. *Polym. Bull.* **1985**, *14* (3–4), 279–286.

(119) Zhou, D.; Khatmullin, R.; Walpita, J.; Miller, N. A.; Luk, H. L.; Vyas, S.; Hadad, C. M.; Glusac, K. D. Mechanistic Study of the Photochemical Hydroxide Ion Release from 9-Hydroxy-10-Methyl-9-Phenyl-9,10-Dihydroacridine. *J. Am. Chem. Soc.* **2012**, *134* (28), 11301–11303.

(120) Zhou, D.; Mirzakulova, E.; Khatmullin, R.; Schapiro, I.; Olivucci, M.; Glusac, K. D. Fast Excited-State Deactivation in N(5)-Ethyl-4a-Hydroxyflavin Pseudobase. *J. Phys. Chem. B* **2011**, *115* (21), 7136–7143.

(121) Sichula, V.; Kucheryavy, P.; Khatmullin, R.; Hu, Y.; Mirzakulova, E.; Vyas, S.; Manzer, S. F.; Hadad, C. M.; Glusac, K. D. Electronic Properties of N(5)-Ethyl Flavinium Ion. *J. Phys. Chem. A* **2010**, *114* (46), 12138–12147.

(122) Lee, C.; Kim, J.; Kim, S.; Chang, Y. J.; Kim, K. S.; Hong, B.; Choi, E. J. Strong Hole-Doping and Robust Resistance-Decrease in Proton-Irradiated Graphene. *Sci. Rep.* **2016**, *6* (February), 1–9.

(123) White, W.; Sanborn, C. D.; Fabian, D. M.; Ardo, S. Conversion of Visible Light into Ionic Power Using Photoacid-Dye-Sensitized Bipolar Ion-Exchange Membranes. *Joule* **2018**, *2* (1), 94–109.

(124) Fonash, S. *Solar Cell Device Physics*, Second.; Elsevier: Burlington, MA, 2010.

(125) Higashino, T.; Imahori, H. Porphyrins as Excellent Dyes for Dye-Sensitized Solar Cells: Recent Developments and Insights. *Dalton Trans.* **2015**, *44* (2), 448–463.

(126) Chang, J.; Ma, C.-J.; Lee, G.; Peng, S.; Yeh, C. Porphyrin-Triarylamine Conjugates: Strong Electronic Communication between Triarylamine Redox Centers via the Porphyrin Dication. *Dalton Trans.* **2005**, No. 8, 1504–1508.

(127) Yu, W. W.; Qu, L.; Guo, W.; Peng, X. Experimental Determination of the Extinction Coefficient of CdTe , CdSe , and CdS Nanocrystals. **2003**, *125* (17), 2854–2860.

(128) Wuister, S. F.; De Mello Donegá, C.; Meijerink, A. Influence of Thiol Capping on the Exciton Luminescence and Decay Kinetics of CdTe and CdSe Quantum Dots. *J. Phys. Chem. B* **2004**, *108* (45), 17393–17397.

(129) Tao, P.; Li, Y.; Schadler, L. S. Transparent Luminescent Silicone Nanocomposites Filled with Bimodal PDMS-Brush-Grafted CdSe Quantum Dots. *J. Mater. Chem. C* **2013**, *1*, 86.

(130) Zhang, H.; Cheng, K.; Hou, Y. M.; Fang, Z.; Pan, Z. X.; Wu, W. J.; Hua, J. L.; Zhong, X. H. Efficient CdSe Quantum Dot-Sensitized Solar Cells Prepared by a Postsynthesis Assembly Approach. *Chem. Commun.* **2012**, *48* (91), 11235.

(131) Jin, W. J.; Fernandez-Arguelles, M. T.; Costa-Fernandez, J. M.; Pereiro, R.; Sanz-Medel, A. Photoactivated Luminescent CdSe Quantum Dots as Sensitive Cyanide Probes in Aqueous Solutions. *Chem. Commun. (Camb).* **2005**, No. 7, 883–885.

(132) Smith, A. M.; Nie, S. Chemical Analysis and Cellular Imaging with Quantum Dots. *Analyst* **2004**, *129* (8), 672–677.